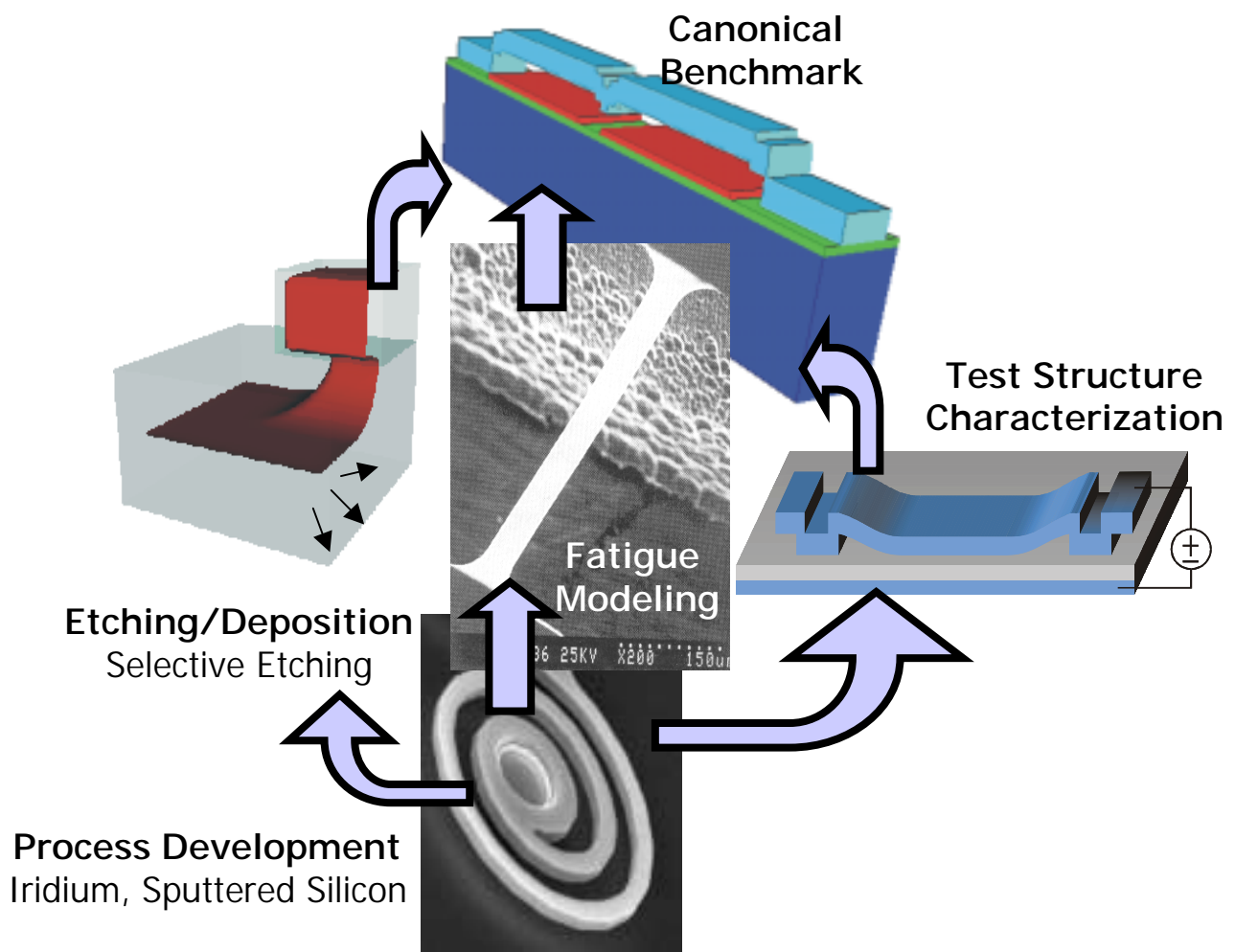


# Advanced CAD System for Electromagnetic MEMS Interactive Analysis (αχαδεμια)



Final Report  
Contract Number: F30600-96-2-0308

# **Advanced CAD System for Electromagnetic MEMS Interactive Analysis (Academia)**

Final Report

Contractor: Stanford University

Agreement Number: F30602-96-2-0308

Project Number: HJ1500-3221-0599

DARPA Order Number: N-7-0504/AO E117/12

Contract Period: September 13, 1996 – October 31, 2000

Sponsor: Department of the Air Force

Technical POC: Robert W. Dutton

Report Prepared by: Robert W. Dutton

## **Forward**

This project titled "Advanced CAD System for Electromagnetic MEMS Interactive Analysis (Academia)" was launched in September, 1996 under support from the DARPA Composite CAD program. The title is somewhat misleading in the sense that while certainly electromagnetic effects are an integral part of MEMS devices, the primary emphasis of the work was focused in the area of electrostatically actuated MEMS beams with primary application for radio frequency (RF) switches. The project was concluded at the end of October, 2000. The following report summarizes key technical achievements, in terms of the three major task areas--software, materials characterization and fabrication of application-oriented MEMS. The report also includes sections that elaborate on added technical details on two points of special importance. First, in the area of computational prototyping of MEMS, results of the software environment for prototyping MEMS are discussed, including opportunities for interactive (web-based) design. Second, material is presented on micro-scale fatigue test structures and characterization of potential new materials use in MEMS. Also included in the report are two appendices that list the publications resulting from this contract (Appendix I) and selected copies of papers that might be difficult to find (Appendix II). Finally, it is important to point out that the most detailed summary of materials from university-based research is found in PhD theses. To date this project has supported more than a half-dozen degree candidates; the PhD thesis contributions of Drs. Guido Cornella (MSE), Edward Chan (EE), and Kenneth Honer (EE) can be cited as a key legacy of the Academia project. Ongoing thesis work of Mr. Kenneth Wang, Mr. Nathan Wilson and Ms. Ping Zhang is expected to provide further contributions that add to the knowledge base being created in support of advanced CAD for MEMS.

# Table of Contents

Forward .....	ii
Table of Contents .....	iii
List of Figures .....	v
List of Tables.....	v
1. Executive Summary .....	1
2. Objectives, Approach and Significant Results.....	2
2.1 Software Development.....	2
2.2 Characterization of MEMS Material Models .....	3
2.3 MEMS Device Modeling and Design.....	5
2.4 Technology Transition of Results.....	7
2.5 References.....	9
3. Software Development.....	10
3.1 A heterogeneous environment for computational prototyping and simulation based design of MEMS .....	10
3.1.1 Introduction .....	10
3.1.2 Simulation environment system requirements .....	12
3.1.3 Internet based prototyping of Micro-Electro-Mechanical Systems.....	13
3.1.3.1 Client-server overview .....	13
3.1.3.2 Client-server architecture .....	14
3.1.4 Geodesic framework.....	16
3.1.4.1 Object repository .....	17
3.1.4.2 Solid modeling module .....	17
3.1.4.3 Level set module .....	18
3.1.4.4 Meshing module.....	18
3.2 Creating geometry for the simulation of Micro-Electro-Mechanical Systems.....	18
3.2.1 Overview .....	18
3.2.2 Previous and current work in geometric simulation for VLSI & MEMS .....	19
3.2.3 Surface representation .....	20
3.2.4 Process emulation vs. process simulation.....	20
3.2.5 Accessibility to algorithms which achieve multiple levels of physical accuracy.....	20
3.3 Examples.....	21
3.3.1 Overview .....	21
3.3.2 Example of creating the canonical RF switch test device .....	21
3.3.3 Example of extending Geodesic – Reactive ion etching .....	26
3.3.5 Example using Geodesic level set module: Process simulation.....	29
3.3.6 Examples of internet based prototyping .....	33
3.4 A solid modeler independent implementation of the Composite CAD Process Definition Specification .....	34
3.4.1 Introduction .....	34
3.4.2 Discussion of commands.....	35
3.4.2.1 Book-keeping .....	35
3.4.2.2 Miscellaneous.....	35

3.4.2.3 Process macros .....	36
3.4.2.4 Process emulation.....	36
3.4.3 Additional notes on implementation of CCPDS inside of Geodesic.....	40
3.4.4 Limitations of the CCPDS standard .....	40
Basic CCPDS .....	41
Level Set.....	41
3.4.5 Summary of CCPDS.....	41
3.5 References.....	42
4. Characterization of MEMS Materials Models .....	44
4.1 Monotonic and Cyclic Testing of Thin Film Materials for RF Switch Application.....	44
4.1.1 Sample Fabrication.....	44
4.1.2 Experimental Setup and Procedures.....	46
4.1.2.1 Micromechanical Testing System.....	46
4.1.2.2 Experimental Procedures .....	47
4.1.3 Results and Discussion.....	48
4.1.3.1 Tensile Test of Pure Al and Al-2%Ti Micro Beams (2 $\mu$ m thick) .....	48
4.1.3.2 Stress Relaxation Test of Pure Al and Al-2%Ti Micro Beams (2 $\mu$ m thick) .....	50
4.1.3.3 Grain Size Study on Pure Al (2 $\mu$ m thick).....	52
4.1.3.4 Inhomogeneous Deformation in Pure Al (2 $\mu$ m thick) .....	53
4.1.3.5 Preliminary Results on Al/Ti co-Sputtered Films(1 $\mu$ m thick).....	54
4.2 In-Situ Stress Monitoring.....	55
4.2.1 Tunneling Sensor and Initial Modeling.....	55
4.2.2 Stress Monitoring Device and Ex-Situ Stress Measurement Results.....	57
4.2.3 Fabrication of Dedicated Stress Monitoring Sensor .....	58
4.2.4 ABAQUS Modeling.....	58
4.3 References.....	60

## List of Figures

Figure 3-1: Typical design loop for a micro-electro-mechanical switch.....	12
Figure 3-2: Schematic of client-server architecture for internet-based prototyping.....	14
Figure 3-3: User interface to web-based MEMS prototyping environment.....	15
Figure 3-4: Geodesic software architecture.....	17
Figure 3-5: Schematic of canonical RF switch and three different SEM views.....	22
Figure 3-6: Model created using process simulation and meshed in Geodesic.....	22
Figure 3-7: CIF file for canonical test device.....	26
Figure 3-8: Idealized reactive ion etch.....	27
Figure 3-9: Schematic of the 4 step process to emulate a reactive ion etch.....	29
Figure 3-10: A conformal deposition of using 3-D levelset process simulation.....	32
Figure 3-11: Example of a selective corner using 3-D leveaset. process simulation.....	32
Figure 3-12: Two examples of mesh generation.....	33
Figure 3-13: Three different MEMS geometries created using Geodesic.....	34
Figure 3-14: Deposit types flow chart.....	37
Figure 3-15: Three types of deposition.....	37
Figure 3-16: Using the offset solid algorithm in Geodesic.....	38
Figure 3-17: Etch types flow chart.....	39
Figure 4-1: Die schematic of a micro beam specimen .....	45
Figure 4-2: SEM micrograph of a free-standing Al micro beam specimen.....	45
Figure 4-3: Top view of components of the custom-designed micromechanical testing system.....	46
Figure 4-4: Stress vs. Strain curves of pure Al and Al-2%Ti micro beams (2mm thick).....	48
Figure 4-5: TEM cross-sectional view of Al <sub>3</sub> Ti.....	49
Figure 4-6: TEM bright filed image of a grain in a pure Al micro beam.....	49
Figure 4-7: TEM bright field image of a grain in an Al-2%Ti micro beam.....	50
Figure 4-8: Stress relaxation of (a) pure Al, (b) Al-2%Ti micro beams (both 2mm thick) .....	51
Figure 4-9: Two-Maxwell-element anelastic model .....	52

## List of Tables

Table 3-1: 12 steps in building the canonical switch .....	23
Table 3-2: File size (in bytes) of four example MEMS devices.....	33
Table 3-3: CCPDS commands organized by functionality.....	35
Table 3-4: Solid modeling commands required to generate geometry .....	41
Table 3-5: Solid model object methods required for model generation .....	41

## **1. Executive Summary**

Simulation and modeling of MEMS devices poses a three-fold challenge: a) difficulties in specifying accurate physical models that include process- and material-dependencies, b) lack of fundamental materials parameters that impact behavior and c) adequate characterization of how the modeling relates final behavior of the devices. In this project a multi-disciplinary team has addressed each of these areas, resulting in significant contributions in all of them. Based on detailed characterization of a MEMS RF switch, used as a canonical benchmarking structure, accuracy (as well as limitations) of current CAD for MEMS has been quantified. A powerful set of algorithms have been developed for specifying MEMS structures, including extensible capabilities for simulation of processing conditions—especially changes resulting from etching and deposition. A new technique for tensile strength measurements of micro-beams has been developed and provides details of grain-scale effects that contribute to failure. FEM-compatible failure models have been developed using extensive data from aluminum beams. Finally, several new MEMS materials that are compatible with conventional CMOS (backend) processing have been explored. The use of sputtered silicon was tested in the context of circuits fabricated with MEMS structures. Other promising materials that have been investigated for MEMS applications include: iridium, titanium-nitride, titanium-tungsten as well as aluminum.

This report is organized as follows. Section 2 gives an overview of the objectives of the project as well as highlight accomplishments in each of these areas. Sections 3 and 4 provide greater discussion of results in the software development and materials characterization aspects of the work. The majority of the results from this research have appeared in conference and journal papers as well as three PhD theses. Appendix I gives a listing of the publications resulting from this work and Appendix II includes reprinted versions of key papers that support the discussion in the text (as well as those that might be more difficult to find in print or which are not available on the web).

## 2. Objectives, Approach and Significant Results

### 2.1 Software Development

A key objective is to develop and demonstrate fully-integrated, FEM-based prototype solver capabilities to model behavior and fabrication process-dependency of MEMS devices. This includes capabilities to consider multi-physics and materials dependencies as well as other process induced factors—for example, geometry effects due to deposition/etching. The overall tool integration strategy was targeted to develop and test key components that overcome limits currently seen to be "bottlenecks" in CAD systems. Application-specific lumped modeling was pursued early on in the project and used to guide the overall direction of the CAD efforts, including improved parameter extraction schemes that cross-link device performance with physical factors such as layout and process dependencies. The approach used here addresses the following information flow and simulation capabilities:

1. Layered access in MEMS specification across levels--layout, process specification, geometry definition, grid and constitutive models
2. Enhanced element technology for discretization of multi-physics systems of equations
3. Unified approach to interface geometry and gridding through use of servers.
4. Demonstration of integrated MEMS simulation capability with internet access to modeling and open interface standards including parameter extraction
5. Prototyping of benchmark canonical RF test structures--both computationally and experimentally--that demonstrate capabilities of models and tools.

The PhD thesis of Edward Chan [1], completed during the course of this project, describes: the validation of a canonical benchmark device (RF switch), characterization of the contact electro-mechanical phenomena, and the design of an electrostatic actuator with an extended range of travel. Included in the thesis are analyses (through simulations) of the effects of: changes in substrate curvature, the influences of stress gradients on fixed-fixed beams, and the importance of considering film coverage in understanding the behavior of composite materials. Rigid-body simulations of the electrostatic actuator with series feedback capacitor, used for extended travel, reveal that tilting always occurs at a spacing of ~60% of the initial gap. This tilting occurs due to asymmetry, but it is unclear why the range does not depend on degree of asymmetry or the size of the series capacitance. One difficulty related to tilting in the electrostatic actuator with extended range of travel is the fact that increasing the feedback or reducing asymmetry cannot mitigate the effect.

Two aspects of the software and design capabilities developed during this research deserve special note and discussion--web-based design of MEMS and accurate modeling of geometry and process-flow information. In the area of web-based design, demonstrations of the final prototype are available through the Stanford TCAD web site [2]. Subsequent to the ending of this contract there has been substantial interest expressed by researchers at the Beckmann Institute at the University of Illinois (Professors Narayan Aluru and Umberto Ravaioli) in continuing efforts in this direction with computational support also coming through NCSA (National Computational Science Alliance) co-located at Illinois. The web-based prototyping environment now includes a more robust interface, remote process tracking to show the status of

submitted jobs, and improvements in the ability to track down errors via the use of error logs. Also demonstrated was an alternative way to view solid models using a Java applet (JGV) developed at the Geometry Center in the University of Minnesota [3]. This complements the use of VRML plug-ins, and provides true platform independence since it requires only a current version of Internet Explorer or Netscape Navigator and no additional plug-ins.

In the areas of geometry modeling and mesh generation, there has been a consolidation of both aspects into an extensible, modeler independent, framework that has been named "Geodesic" [4]. Geodesic is being released in source code form to the MEMS community through the Stanford TCAD web site [2]. The framework is built using the Tcl/Tk language interface to the Visualization Toolkit (VTK) and provides a generic scripting interface layer to the Shapes and Parasolid solid modeler libraries. This interface layer has been designed to provide capabilities independent of the solid modeler kernel being used. It also facilitates extension to other solid modeling kernels (e.g. ACIS). Geodesic can be used as a "black box" geometric-based process simulator for MEMS structures, taking a mask set in CIF format and a process specification in the Composite CAD Process Definition (CCPDS) format and generating solid models which can then be meshed using commercially available tools (e.g. MEGA from SCOREC).

In addition to the geometry-only algorithms suggested by the CCPDS format, Geodesic also provides the ability to incorporate physically-based process simulation using either external simulation programs or through an integrated 2D/3D level set kernel for boundary motion. The significant features of the level set kernel include: a) a modular level set software structure, developed to support interchangeable grid schemes and boundary movement functions; b) general 3D selective etch modeling capabilities; c) a compressed data structure, developed to reduce memory requirements; d) demonstration of techniques for distributing computation on compressed data structure in a heterogeneous computing environment.

## **2.2 Characterization of MEMS Material Models**

The objective of this task is to develop extraction schemes for materials properties using simplified MEMS test structures. In combination with the CAD tools efforts, the physical models (including microstructure) have been evaluated and modified as needed. The scope of material characterization efforts include both standard metal layers (possibly graded as well) and reliability issues such as plastic yield and fatigue. The extraction and validation steps for physical models is a key link with the other two tasks. The approach used in this work builds on the following themes:

1. Mechanical characterization of MEMS materials with dependencies on processing and microstructure.
2. Reliability studies including both fracture and fatigue.
3. Feedback to the constitutive models in the FEM-based modeling task.

This task had two component activities--fatigue modeling (including measurement) and efforts to develop an in situ stress monitoring structure. The fatigue modeling efforts were highly productive in terms of new techniques and quantitative information about this serious reliability

concern for MEMS. The following gives a summary of highlight results, particularly coming from the PhD thesis work of Guido Cornella. The proof-of-concept for in situ stress monitoring was only partially successful; a variety of limitations in process control during fabrication resulted in this aspect of the project being terminated. A summary of limited results for in-situ stress monitoring are given in Section II. The PhD student, Ms Ping Zhang, shifted her thesis topic to further studies in the area of fatigue measurements and modeling. This area is of great ongoing importance to the MEMS field, especially of value to DoD. Currently there is no follow-on support for these studies.

In the PhD thesis by Guido Cornella [5], a new measurement method and design of test structures for fatigue modeling of micron-scale MEMS beams has been developed. Cyclic and static relaxation tests at various strains have been performed for Al micro-beams of different thickness. The results of this study have allowed the construction of stress-strain curves for both cyclic relaxation and static relaxation. These new curves help to infer how the material behaves due to cyclic loading, vis a vis a single application of stress. In addition a post-test sample extraction procedure has been developed which allows the removal of tested, but not fractured microbeams without application of additional loads, allowing one to "freeze" the dislocation arrangement which has evolved throughout testing. Moreover, TEM sample preparation techniques have been developed that allow one to investigate (and illustrate) dislocation states within the tested samples. TEM analysis of cyclically loaded samples reveals the evolution of the dislocation arrangement with the number of loading cycles. At first dislocations interact and entangle; later they form dislocation networks within a grain. Upon further cycling this dislocation network expands and eventually reaches across multiple grains.

Tensile tests on aluminum micro-beams of four different thickness values were performed at strain rates between  $7.6 \times 10^{-2}/s$  and  $7.6 \times 10^{-6}/s$ . Strain rate sensitivity has been observed for all film thickness values. Results for small strain rates in the nominally linear-elastic regime (at small strains) deviate considerably from linear elastic behavior. The observed characteristics are well described by anelastic material behavior. Anelastic reloading after stress relaxation experiments supports the anelasticity hypothesis. A two-mechanism model with a fast and a slow relaxation time -corresponding to recoverable grain boundary sliding and dislocation motion - has been developed to explain the observed relaxation behavior in Al thin film samples during monotonic and cyclic loading. The 1D implementation and testing of the model has been performed using ABAQUS; the basic model formulation is also suitable for 2-3D applications.

Iridium thin film samples have been tested under monotonic and cyclic testing conditions. Linear-elastic behavior has been observed up to fracture. Unloading of iridium samples has shown no hysteresis of loading and unloading curves. Fracture stresses of up to 3.5 GPa and fracture strains of up to 0.75% have been measured. A Young's modulus of 490 GPa as compared to the literature value of 528 GPa (7.2% deviation) has been extracted. Cyclic loading experiments of iridium microbeam samples showed small relaxation of the peak stress at the initial strain (around 10%). This initial relaxation cannot be explained by anelasticity since reloading is not observed at the end of the test. The relaxation is more likely due to plastic

deformation. No relaxation of the peak stress was observed for further cyclic testing on the same sample at increased strains.

In addition, alloyed Al beams with about 2% Ti were studied, deposited as 7-ply of Al(0.5micron):Ti(10nm) multilayers and then annealed at 550C for 1hr. It was found from TEM studies that small particles of Al<sub>3</sub>Ti form along the grain boundaries of Al after the annealing. In monotonic tensile testing, the Ti-alloyed beams showed 200MPa of yield strength, which is at least 80% higher than pure Al beams. They also exhibit about 2.5% elongation--much larger than that of pure Al. This alloy effect is potentially of practical importance because one can fabricate much stronger Al beams without substantially sacrificing the conductivity. Relaxation in the pure Al case is much larger than the case of the alloyed samples probably due to precipitation at the grain boundaries which hinders grain boundary motion. Relaxation found in this case is much larger than those previously reported in the case of bulk or thin films on substrates.

### **2.3 MEMS Device Modeling and Design**

Design and implementation of MEMS structures, including materials parameter extraction, were used to test the CAD and physical models based on MEMS devices of interest to DoD. The experimental measurements made with these structures helped to facilitate the critical evaluation of models, physical parameters and overall simulation accuracy of CAD for MEMS devices. The test vehicles from this component of the research also supported canonical benchmarking of both new materials for MEMS and accuracy of Composite CAD in MEMS applications, specifically the RF switch. The approach used in this work builds on the following themes:

1. Design/implementation of test structures for materials characterization.
2. Concurrent building of prototype MEMS application devices (RF switch).
3. Measurement, parameter extraction, and testing of CAD models.

Prototype development, evaluation and documentation of CMOS-compatible MEMS process integration that is capable of exploiting alternative materials (vis a vis standard poly-silicon used in MUMPS) ended up to be the major outcome of this task. The primary materials of interest centered on standard CMOS-oriented materials (i.e. sputtered silicon) but also included alternative, potential break-through materials such as iridium. DoD system-level applications of RF MEMS and initial evaluation of process integration and test structure work were initiated based on collaborations with AFRL (Hanscomb AFB). However, due to lack of funding specifically in that area and loss of personnel from this task (to local start-ups), the detailed DoD application testing portion of the work ended prematurely.

Several criteria must be met in order to create a functional RF MEMS device. These criteria include controllable stress, high electrical conductivity, and mechanical stability. Integration with circuitry may also be important for some applications. The importance of mechanical stability, particularly in regards to strain gradients was highlighted by this work on test structures.

Low stress films were achieved in a variety of materials using DC magnetron sputtering and ion-gun evaporation. In DC magnetron sputtering, stresses were controlled by adjusting the deposition power and working gas pressure. Using this method it was possible to achieve stresses lower than 100 MPa in sputtered aluminum, silicon, titanium, titanium-nitride, and titanium-tungsten. In ion-gun assisted evaporation, a source of charged particles is directed into the flux of atoms coming from the target. This modifies energy and direction of incoming atoms, changing the atomic peening effect at the substrate. Using this method, it was possible to vary the stresses in iridium and platinum.

Due to relatively low mechanical resonant frequencies ( $< 1$  MHz), most electrostatic MEMS do not require high levels of conductivity. RF MEMS, by contrast, have more stringent requirements in this regard. Sputtered aluminum and nickel-molybdenum multilayers are much more conductive than titanium and its alloys or silicon. However, nickel-molybdenum multilayers are more difficult to pattern and etch than these other materials and pure aluminum is typically unsuitable because of issues with its mechanical properties.

Aluminum displayed a tendency to warp when released from its sacrificial layer. It was found that the release parameters played a dominant role in this warping and that there were large variations in the radius of curvature of the final structures, even among adjacent devices. Design and process techniques to reduce the impact of released curvatures on electrostatic parallel plate devices were explored and evaluated. Using these techniques, it was possible to successfully release aluminum-based variable capacitors. However, when operated as a switch, the on-off capacitance ratio of these devices was limited by warping in the structure. Pure aluminum also demonstrated strong anelastic behavior [5] which, even if the devices could be made perfectly flat, would result in inconsistent operating voltages when used in an RF switch. Aluminum alloyed with two percent Titanium showed much better behavior in this regard, as discussed in the Section 2.2.

On-chip integration of circuitry with Micro-Electro-Mechanical Systems (MEMS) components is vital to the performance of many types of microsensors. To date, the most common material for integrated surface micromachining has been LPCVD polysilicon, which is deposited and annealed at temperatures that are incompatible with pre-fabricated standard CMOS circuitry. This has required modifications to the CMOS process or fabricating the structural layers before processing the electrical circuitry, resulting in increased complexity. Sputtered silicon, by contrast, can be deposited directly atop CMOS circuitry at very modest temperatures. Although not as conductive as aluminum, silicon has been proven acceptable for a wide variety of applications.

Sputtered silicon microstructures were made using oxide and polyimide sacrificial layers. Films deposited atop oxide were wet-released in buffered HF. It was discovered that sputtered silicon was permeable to buffered HF at film thickness of up to 5 microns. Using this permeability, buried cavities were made in underlying oxide layers. Films deposited above the polyimide were dry-released in an oxygen plasma. The dry-release eliminated the need for critical point drying

normally required to prevent stiction caused by capillary forces during the wet release process. Released curvatures of sputtered silicon cantilevers were more consistent than in aluminum cantilevers. However, the curvatures were dependent on thickness. A model based on surface stresses as the dominant source of the strain gradient in the films was proposed and predicted a released radius of curvature proportional to thickness squared, matching empirical results.

Several additional properties of sputtered silicon films were investigated, including their in-plane stress ( $< 100$  MPa), density ( $2.24 \pm 0.09$  g/cc), surface roughness (3 nm RMS), and electrical resistivity ( $> 6$  Mohm/square). Improvements in the electrical conductivity of completed structures were realized by cladding the sputtered silicon structural layers in symmetric, 50 nm thick layers of titanium-tungsten.

The dry-release sputtered silicon process was integrated with pre-fabricated CMOS transistors and did not change the maximum saturation current by more than 3%; there was no significant difference apparent in subthreshold operation. As a demonstration, the dry-released TiW-clad sputtered silicon process was used to make an electrostatically deflected plate structure with integrated capacitance measurement circuitry, the output of which was correlated to deflection. This work represents the first application of sputtered silicon to integrated MEMS. While not of sufficient conductivity to be used in RF MEMS applications, sputtered silicon is a potential replacement for LPCVD polysilicon and demonstrates the feasibility of integrating CMOS circuitry with sputtered MEMS devices. Further technical details are available in the PhD thesis of Ken Honer [6] as well as the IMECE '99 conference paper [7]. An invention disclosure on the sputtered silicon process has been filed with the Stanford's Office of Tehnology Licensing.

#### **2.4 Technology Transition of Results**

The results of this project have been transitioned to others--academic, government and industry--primarily through published work in conferences, journals and PhD theses. In each of the task areas there have been major advances as reflected in three PhD theses to date [1][5][6] and a fourth expected to be completed in 2001 [8].

The software aspects of this project have resulted in two prototypes that have been demonstrated at DARPA contractor meetings and program manager site visits as Stanford University. There also have been a variety of interactions with CAD vendors involved in the Composite CAD program, many of these have directly supported commercial developments--both in terms of providing prototype modules as well as critical benchmarking information. One example of particular significance in the area of standards for the Composite CAD program has been the independent testing (and implementation) of CCPDS as discussed in Section 2.1. This implementation is also included within the Geodesic software prototype that is available through the Stanford TCAD group's web site [2]. There has been a sustained set of interactions with Microcosm (and also Coyote Systems, now merged with Microcosm), especially in the areas of geometric modeling and internet-based MEMS prototyping.

While the main efforts and emphasis to date in technology transition for the software has focused primarily on the Composite CAD vendors, two recent sets of interactions show excellent

prospect for future impact. In Section 2.2 the interactions with Beckmann Institute at the University of Illinois was mentioned. The combination of researchers at Beckmann with interests in MEMS and the computational resources provided through NCSA, offer a very potent option for the ongoing development of interactive MEMS design using a web-based paradigm demonstrated in this project. Professor Narayan Aluru, also active in other DARPA programs in the MEMS area, has expressed interest and willingness to go forward in this area; our Stanford team has offered to assist him both in obtaining our code and collaborative efforts to move further in this research direction.

The second aspect of ongoing technology transition for software results from this work involved the Focus Research Center (FRC) in the area of interconnects, sponsored through MARCO (including a substantial component of DoD funding) and headed by Professor James Meindl of the Georgia Institute of Technology. Specifically, the capabilities that have been developed under this program in terms of the Geodesic prototype are potentially of major use and benefit in modeling interconnections in VLSI. This includes options for 3D integration of heterogeneous, mixed technology capabilities as part of interconnect fabrics. Specifically, the ability of Geodesic to deal with complex geometries that include process and technology dependencies--the goals related to MEMS--turns out to be nearly ideally suited for the applications in interconnect domain. Hence, with strong support and encouragement from Professor Meindl, the Geodesic prototype will be used and further extended under the ongoing MARCO FRC in interconnects.

There have been several interactions in testing advanced RF MEMS structures that can be applied to DoD-oriented applications and that have been leveraged by test structure work and leading edge processing capabilities for MEMS at Stanford. Test device work was carried out in collaboration with the group headed by Captain Rob Reid (AFRL/Hanscomb). As described in Section 2.3, these efforts have been curtailed in scope pending new funding sources. There have also been extensive discussions between Professor Greg Kovacs and staff at Hughes (HRL) to determine feasibility for developing SOS/CMOS to demonstrate that Stanford photovoltaic actuation technology that could be integrated with MEMS. The devices have already been shown to actuate an HRL RF MEMS switch using Stanford microphotovoltaics. Despite the sporadic nature of both AFRL and HRL interactions there have been very real benefits to both groups leveraged through this research program.

## 2.5 References

- [1] Edward Keat Leem Chan, "Characterization and Modeling of Electrostatically Actuated Polysilicon Micromechanical Devices," Stanford University PhD Thesis, November, 1999.
- [2] <http://www-tcad.stanford.edu/~mems/>
- [3] N. M. Wilson, K. Wang, D. Yergeau, and R. W. Dutton, "GEODESIC: A New and Extensible Geometry Tool and Framework with Application to MEMS", Technical Digest, Modeling and Simulation of Microsystems (MSM) Conference, March 27-29, 2000.
- [4] Guido Cornella, "Monotonic and Cyclic Testing of Thin Film Materials for MEMS Applications, " Stanford University PhD Thesis, July, 1999.
- [5] Kenneth Honer, "Surface Micromachining Techniques for Integrated Microsystems," Stanford University PhD Thesis, January, 2001.
- [6] K. A. Honer and G. T. A. Kovacs, "Sputtered Silicon for Microstructures and Microcavities", International Mechanical Engineering Congress and Exposition, Nashville, TN, USA, November 1999.
- [7] Kenneth Wang, "Level Set Methods for Computational Prototyping with Application to Hemodynamic Modeling," Stanford University PhD Thesis, Expected Date, 2001.
- [8] <http://www.geom.umn.edu/java/JGV/>

### 3. Software Development

**Authors: Nathan Wilson, Dr. Daniel Yergeau, Prof. Robert W. Dutton.**

#### 3.1 A heterogeneous environment for computational prototyping and simulation based design of MEMS

##### 3.1.1 Introduction

Micro-Electro-Mechanical Systems (MEMS) offer dramatic new functional capabilities. Analysis of MEMS is a challenge; the structures are geometrically complicated, electromechanically coupled, and inherently three-dimensional. The multi-domain physics for MEMS includes: electrical, mechanical, and fluidic interactions. Effects of each domain need to be accurately simulated to correctly predict device performance. In addition, IC-based fabrication techniques require the modeling of complex material behavior and processing such as etching, deposition, and thermal processes such as diffusion (and oxidation). The size and aspect ratios of typical MEMS structures differ significantly from those traditionally found in the VLSI community. This spatial stiffness makes it difficult to construct a geometry model using standard process simulation tools.

Several leading authorities in the field believe that design tools are critical to the future and the growth of the MEMS market. For example, Karen W. Markus, director of the MEMS Technology Applications Center at MCNC has stated [1]:

*MEMS foundries cannot effectively serve their customers without a set of engineering design tools that enable remote, non-expert, users to interface with those foundries. There are no such packages that free the designer from needing a comprehensive understanding of the fabrication process or the nuances of polygon-level layout design.*

In addition, Eric Peeters from Xerox writes [2]:

*Several microelectromechanical systems have achieved commercial success. The barriers can still be formidable, though, and the path to success is often much different for MEMS than it was for mainstream semiconductors. Maturing software for comprehensive modeling and design will help in the future.*

Stephen Senturia, a leading expert in the field of MEMS simulation commented on the state-of-the-art in [3]:

*Technologies for fabricating a variety of MEMS devices have developed rapidly, but computational tools that allow engineers to quickly design and optimize these micromachines have not kept pace. Inadequate simulation tools force MEMS designers to resort to physical prototyping.*

In the MEMS field, it is becoming widely accepted that representing the 3-D geometry of devices is critical for simulation based design. Many commercial and academic systems for MEMS analysis rely on purely geometric operations to create the structures. Notable examples include MEMCAD, Intellicad, and Solidis [4-8]. While tools exist for creating geometry for the VLSI community, there are unique challenges posed by MEMS. Modeling challenges include the complexity and aspect ratios of typical structures, residual stresses which create initial curvature in ideally flat devices, and effects of the materials used. The typical dimensions of MEM switches (such as fabricated using the MUMPS process) are on the order of several hundred microns in length, a width on the order of 1/10 the length, and thicknesses of only several microns. These dimensions cause significant problems for deposition and etching process simulators such as SPEEDIE [9]. If full 3-D physical process simulations were performed, it would take excessive amounts of computing resources including time and memory that exceed current limitations of software and hardware. In addition, commonly occurring features such as large flat regions do not gain geometric accuracy from 3-D deposition and etching simulation compared to using 1-D or 2-D simulation.

A second issue concerning micro-system simulation is that available commercial tools are designed for a “traditional” computing environment. A traditional computing environment consists of a single user working at a fixed workstation running software locally with licenses tied directly to the given machine (or local cluster of machines). Commercial micro-system design tools were not designed to minimize platform dependence or take advantage of the latest technology (e.g. the internet). The field of MEMS provides an ideal target for internet-based simulation software for the following four important reasons:

1. *Emerging market.* Unlike the automotive and aerospace industries which have been around and utilizing simulation tools for decades, the MEMS market is relatively new and use of simulation in the design process has not yet become deeply entrenched using existing simulation paradigms.
2. *Cost.* The automotive and aerospace industry are driven by a few large companies that can devote significant manpower and financial resources to computational prototyping. In sharp contrast, MEMS is a field driven by smaller firms and universities with more financial constraints.
3. *Size of models.* A typical model for an aircraft involves millions of unknowns (i.e. degrees of freedom). However, many micromechanical devices of interest can be reasonably simulated with tens-of-thousands of degrees of freedom.
4. *Standardized processes.* Due to inherent difficulties in IC fabrication, several popular commercial processes (e.g. MUMPS) currently exist. Since fabrication runs take several months, significant time is lost between runs if one is iteratively designing a prototype. This provides opportunities for “virtual fabrication runs” which can be done using internet-based simulation tools in between fabrication of devices.

This report documents a MEMS computational prototyping system which was developed from the ground up to take full advantage of state-of-the-art technology in computer hardware, software, and the internet. Key design decisions in the software architecture and engineering

tradeoffs of computational efficiency for automation were made to enable internet-based prototyping. After discussing the needs of the typical microsystem developer, an overview of the system is given. Novel methods are documented which utilize existing tools in a computationally efficient method to achieve accurate and practical geometry.

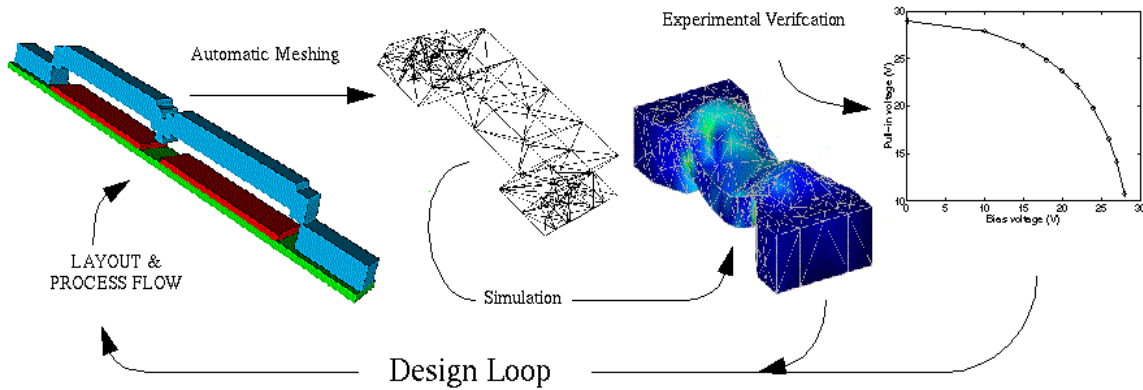


Figure 3-1: Typical design loop for a micro-electro-mechanical switch.

### 3.1.2 Simulation environment system requirements

The architecture of a software system for microsystem design must take into account the needs and skills of a typical designer. Market research indicates typical MEMS design groups are small, without individuals who are solely dedicated to computer simulation [10]. Here several basic assumptions can be made of the typical designer:

- Mechanical/Electrical engineer with a masters or equivalent work experience
- Minimal background in computer simulation
- Desire to utilize new tools which supply useful and timely feedback on new designs

The potential users are then designers who want to use computer simulation to help guide their development efforts. Under these assumptions, Fig. 3-1 shows a desired iterative design cycle for a RF switch. In general, a simulation based design system for MEMS devices consists of four major components:

1. Geometry Definition
2. Discretization (i.e. mesh generation)
3. Simulation (e.g. coupled electro-mechanical)
4. Visualization (e.g. displacements, charges, stress)

These components need to be sufficiently integrated so that information can travel from one module to another without significant user intervention. Two quite different modeling methodologies are being pursued among the MEMS CAD community. The "homogeneous" approach is to develop tightly integrated component simulation tools and design methodology. Alternatively, a "heterogeneous" approach is one that wraps distinctly different end-user software packages to create a "meta" tool. The MEMCAD system is one well known example that uses commercial and other academic tools (ABAQUS, IDEAS, and Fastcap) [4]. The system detailed below relies on using a heterogeneous collection of appropriately chosen external software packages to create a versatile system which provides maximum automation of the model creation and simulation process.

### **3.1.3 Internet based prototyping of Micro-Electro-Mechanical Systems**

This work included a preliminary investigation internet-based simulation of microsystems. It focused on using mainstream, current web-based technology while highlighting possible future directions in relevant internet technology. It proposed a paradigm of automation that limits the information that needs to pass back and forth between a browser-based client and the back-end server. In the present implementation, geometric models are generated from layouts and a process specification, then meshed automatically, and simulated using *hp*-adaptive finite element techniques. The web- and browser-based environment provides file transfer, simulation control, and visualization of simulated results.

#### **3.1.3.1 Client-server overview**

The system takes advantage of a client-server paradigm as shown schematically in Fig. 3-2. The yellow boxes (masks/layout, processing flow, boundary conditions, and material properties) indicate the user provided information. The left side of the diagram also indicates the steps that are carried out on the designer's machine (referred to as the "client"). The right side of the figure corresponds to the processes run on the "server." The server can be the same machine as the client, a different machine on the same local network, or a remote machine accessed via the internet, even through a proxy. There are three main steps carried out on the server:

1. *Geometric Modeling*. This step takes the user-defined process flow and masks for the layout and creates a solid model representing the three-dimensional device.
2. *Discretization*. This step automatically breaks the solid model into smaller non-overlapping discrete pieces (called a mesh) needed for simulation.
3. *Simulation*. This step simulates the device using multi-physics Finite Element Analysis techniques to obtain electrical and mechanical characteristics of the structure.

In the overall system, the boxes on the left correspond to computational inexpensive tasks, while the boxes on the right can require significant computational resources. The communication between the left and the right side is transaction oriented (not interactive) and thus can be done efficiently by transmitting small- to medium-sized blocks of data.

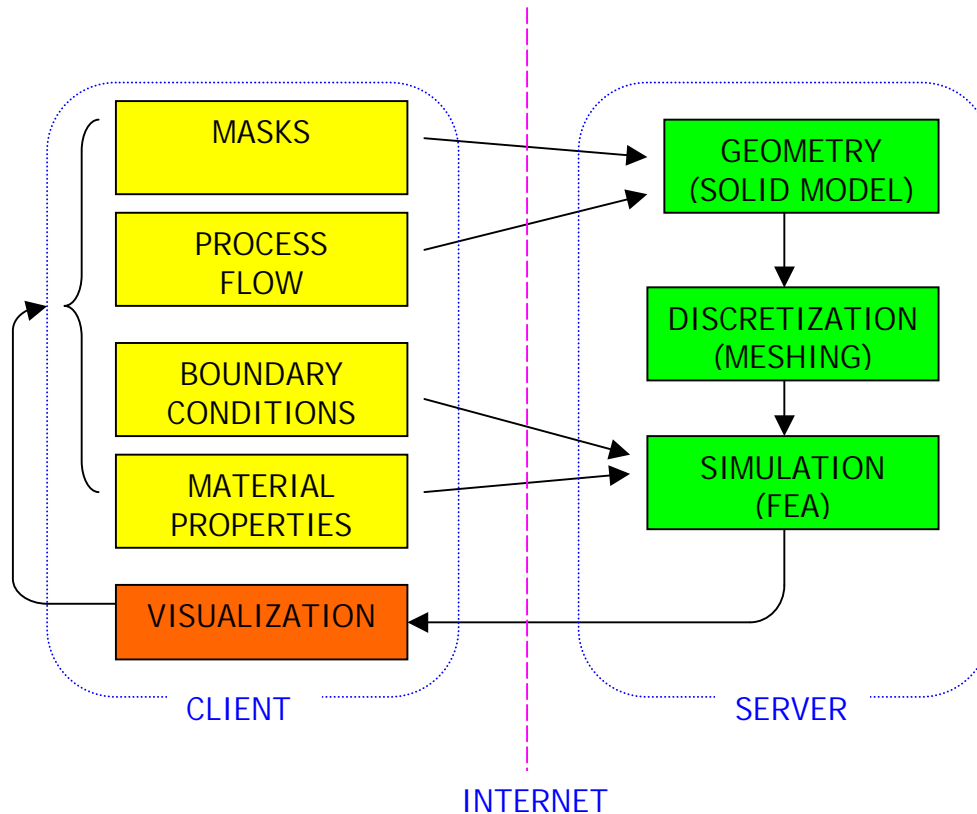


Figure 3-2: Schematic of client-server architecture for internet-based prototyping.

### 3.1.3.2 Client-server architecture

The client side application is presented through a standard frames-capable web browser as seen in Fig. 3-3. The toolbar on the left allows selection of several submenus, which in turn update the toolbar and/or the main viewing window to guide the user interactively through the process of going from a design to device simulation. Most of the submenus consist of dialogs for information entered directly using standard HTML form objects. The information is transferred using standard HTTP POST/GET methods and server-side CGI scripts. The use of these standard transaction mechanisms permits access to a server across a firewall, provided that an HTTP proxy is available.

As an example transaction, consider the required step of passing the layouts created on the user's local machine to the server for geometric modeling. Typically the masks will be created in a standard layout editor (e.g. L-Edit, Magic, etc.) and exist on the client machine in the form of a text file. The user will then specify the desired filename in a standard HTML form object that uses the HTTP POST method to pass the information to the server. The server receives this information via the HTTP port and runs an appropriate CGI script to create a copy of the file on the server. An identical mechanism can be used to transfer a file containing the fabrication process flow (using the the Composite CAD Process Definition Specification [11]).

The user interface was implemented primarily with standard HTML, instead of Java, for greater portability among browsers and to avoid some of the security restrictions of Java (i.e. Java applets cannot access the local filesystem which would have prohibited uploading of local files containing mask and process flow information). Unfortunately, the transaction-oriented nature of HTTP introduces latencies that are too large for highly interactive use. Tasks such as visualization that require a high level of interactivity or do not map well into a forms-based interface are implemented using Java applets that are downloaded to the browser. Examples of applets utilized in this implementation include an interactive geometry visualization applet (JGV) discussed below and a user friendly applet to create a process flow. The process flow applet uses an HTTP POST method to communicate with the CGI scripts on the server for reasons stated above.

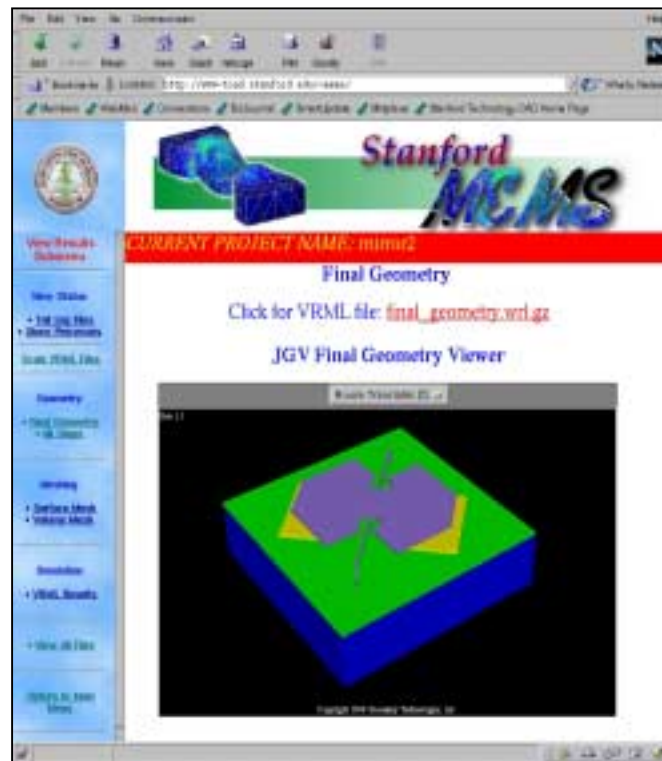


Figure 3-3: User interface (i.e. a web-browser) to web-based MEMS prototyping environment.

Visualization of geometry and simulation results on the local machine is an important step in the design process. Several visualization techniques were tested. First, visualization of the geometry and the surface meshing was achieved using the Virtual Reality Markup Language (VRML) [12]. VRML was one of the first standard file formats proposed for 3-D internet-based visualization. Unfortunately, the standard was never universally adopted and VRML viewers are typically limited to only a subset of the functionality and are not available on all platforms. The VRML standard is no longer being developed, and the Web3D consortium has migrated its

efforts into developing a new extensible 3-D format [13] for internet applications. The second attempt for portable geometry and mesh visualization was to use a visualization package named JGV [14], an applet implemented in pure Java. The viewer was less elaborate than the VRML viewers, but did not require special plugins and is only 100 kilobytes in size, small enough to be transmitted with the geometry over low bandwidth links such as a 56 Kbps modem.

The server side framework is implemented as a collection of PERL and Tcl CGI scripts that manage the transmission and storage of data and control other simulation tools on the server. To organize the information maintained on the server, the idea of a “project” is employed. A project consists of all of the files needed as input (e.g. process flow and masks), the desired output files of the simulation tools (e.g. visualization files), files that maintain the current state of the device (e.g. if mesh generation is completed), and log files (e.g. files detailing the success or failure of a desired operation). Currently this is handled transparently to the user by having the server track the needed files and storing them physically in a single directory for the given project. The client controls the projects via a submenu in the interface that permits the fundamental operations of creating, deleting, renaming, and copying a project. The user is constantly reminded of the current project name since it is clearly displayed in a separate frame of the web-browser (see Fig. 3-3). Since the server tracks the varying states of projects, the user can change between projects or interact with multiple projects via addition windows of the web browser. The main application called by the server scripts, named Geodesic, is detailed in the following section.

### **3.1.4 Geodesic framework**

Geodesic consists of an extensible framework to create MEMS geometry of varying degrees of physical accuracy using multiple geometric simulation techniques. It has an integrated meshing layer that permits automatic tetrahedral mesh generation. In addition, it can create input files automatically for a finite-element code, based on the ProPHLEX finite-element kernel [15], which permits *hp*-adaptive finite element simulation of the coupled electromechanical problem. Fig. 3-4 depicts the architecture of Geodesic. The input to Geodesic consists of a set of masks (defined in a CIF file) and a process flow (specified using the Composite CAD Process Definition Specification [11]). The geometry is then built in a layer by layer fashion by emulating and/or simulating the processing steps used to build the actual device (i.e. “virtual fabrication” or “vfab”). Currently only geometric steps are supported, though these are sufficient for the devices targeted by this contract. When fabrication steps such as implants and diffusions alter the mechanical behavior of the device, they can be approximated by using distinct geometric regions for regions of significantly different doping.

The challenges of integrating diverse tools such as solid modelers and mesh generation software into a unified framework involves tasks of varying computational expense and algorithmic challenge. In addition, in a research setting it is desired to have a tool that permits rapid prototyping and quick testing of new algorithms. For this reason, Geodesic uses Tcl/Tk as a front-end integration environment. Tcl/Tk combines the ease of a powerful scripting language with the ability to imbed C/C++ code for computationally intensive operations. There are four

main modules in Geodesic: the object repository, the solid modeling module, the levelset kernel, and the meshing interface.

### 3.1.4.1 Object repository

The object repository is a simple hash table of names (character strings) with corresponding object pointers. The repository allows for the basic operations of adding, deleting, listing, and querying of object type. This layer does not know or care about the underlying structure of the objects contained in it, it merely returns the pointers and calls instantiation and deletion methods as required.

### 3.1.4.2 Solid modeling module

At the heart of geometric modeling is a solid modeler. By wrapping the solid modeling function calls used in generic interface layer, Geodesic can be used with multiple solid modeling kernels. Because these packages inevitably exhibit relative strengths and weaknesses, it is useful to design for a plug-and-play modularity which enables the easy exchange of one implementation for another. This interoperability with multiple kernels is facilitated by designing the system to minimize the number of distinct function calls required to build a geometry. The current implementation can be used with two different commercial solid model kernels (Shapes [16] and Parasolid [17]). So far, only limited results have been achieved using a freely available solid

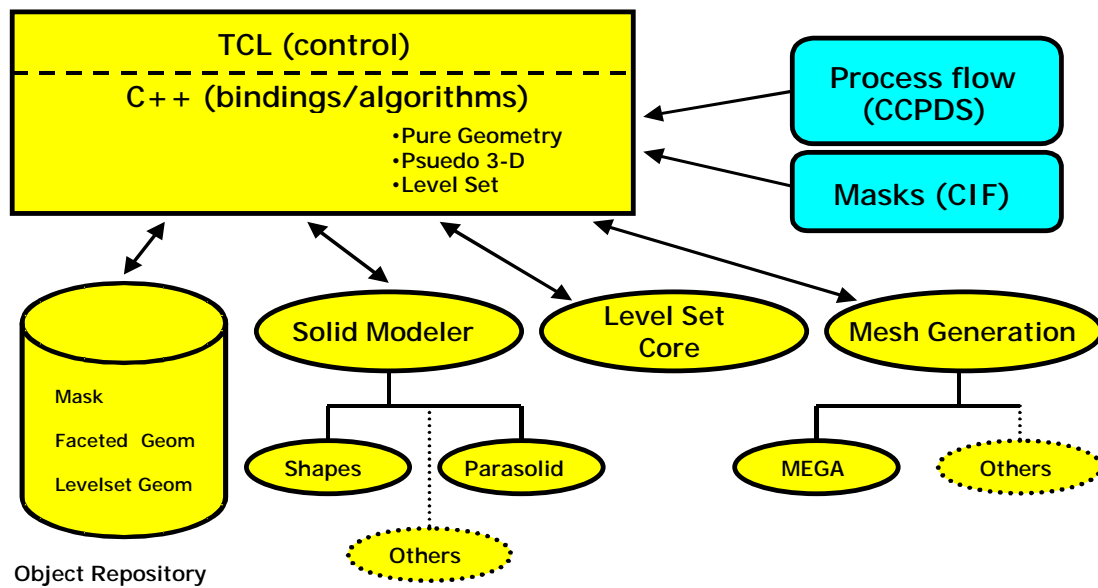


Figure 3-4: Geodesic software architecture.

modeler (IRIT [18]) due to limitations in its internal data representation and capabilities. The extension of Geodesic for use with other solid modelers (e.g. ACIS [19]) should be straight forward.

### **3.1.4.3 Level set module**

Geodesic contains a fully integrated general multi-dimensional level set kernel which can be used for physical process simulation [20]. Briefly, the level set method refers to a mathematical formulation which represents the motion of a propagating curve in the form of a partial differential equation (PDE) which is evolved in time. The equation solves the evolution of a scalar field that implicitly represents the propagating interface. The level set method has many advantages over traditional Lagrangian techniques used to track interfaces (i.e. string methods, marker particle techniques, etc.) in that the method naturally allows for topologic change, and the extension to higher spatial dimensions is straightforward. One of the major difficulties in physical process simulation using the level set method involves defining appropriate physics-capturing velocity functions for different deposition and etching processes. Several cutting-edge techniques are employed in the level set implementation found inside of Geodesic. These include using a compact storage scheme to reduce memory requirements and a technique known in the literature as “narrow-band level set methods” that greatly reduce the computational requirements. The integration of this module with the rest of the Geodesic system enables level set based modeling to be done in conjunction with the other geometric techniques described below.

### **3.1.4.4 Meshing module**

Geodesic also contains a generic meshing layer. In the current implementation, only the MEGA automatic mesh generation package [21] is supported. Its functionality includes “meshing through the thickness,” which is useful in the simulation of thin material layers frequently encountered in MEMS. It also possesses special boundary layer meshing capabilities useful in microfluidics. See [22] for details on automatic mesh generation for microsystem simulation.

With the overview of the Geodesic framework complete, more detail is now provided on building geometry appropriate for microsystem simulation. The task of creating the geometry involves the solid modeling module and can involve the level set module as detailed below.

## **3.2 Creating geometry for the simulation of Micro-Electro-Mechanical Systems**

### **3.2.1 Overview**

In the field of microsystems, numerous commercial and academic efforts are underway to develop simulation based design (SBD) systems [4-8]. These systems used assorted methods to generate geometry for MEMS electro-mechanical simulation. All of these systems currently rely purely on geometric operations to create geometry. That is, there is no physical process simulation involved or used in creating the geometry of a micro-mechanical device. These tools commonly refer to their operations as “process emulation,” which implies that the user must know certain characteristics of the final geometry. More specifically, the user must at a minimum specify layer thicknesses, etching masks, and a simplified process flow. On the other

hand, process simulation allows the user to specify an input topology and a physics-based model will evolve the geometry based on process specific parameters such as etch rate, selectivity, sticking coefficients, etc. Thus, a user must be able to characterize a processing step and feed the simulator the appropriate parameters, but characteristics of the final geometry are not specified. The interested reader can refer to [23] for a brief history of process simulation and its application.

When one considers utilizing MEMS geometry, there is an important distinction between creating geometry for visualizing the outcome of processing steps and using geometry for simulation. In the case of visualizing the geometry, a designer may be curious what his device will actually look like given the masks and processing steps he has specified. Visual inspection may lead to the discovery of design rule violations, obvious design errors such as missing supports, inappropriate layer thicknesses based on prior knowledge of similar devices, etc. In the visualization of the geometry, the retention of small features in a device will have little impact on the ability of the designer to work with it. That is, even the most detailed devices that will be discussed below can comfortably be viewed interactively on a modern PC or workstation. However, in stark contrast, the retention of small features in the geometry which do not impact the global behavior of the device can be extremely computationally costly in simulation. For example, the retention of etch release holes in a device that do not affect the ultimate performance of the device may not be hard to visualize, but may make the mesh generation and the simulation of the device take CPU days instead of CPU hours to perform.

Although the issues are similar in devices for microfluidics and thermally actuated devices, the focus of this work was on generating geometry for the electro-mechanical simulation of microsystems. This is reasonable since there is a large number of devices that perform in this physical domain (e.g. RF switches, comb drives, etc.) and electro-mechanical devices also provide a rich set of devices with varying types of geometry. The goal was to develop a versatile software framework which permits the creation and utilization of varying degrees of topologic complexity and geometric physical accuracy as required for simulation.

### **3.2.2 Previous and current work in geometric simulation for VLSI & MEMS**

Interest in automating 3-D geometry construction, using only mask and process information, for VLSI and MEMS applications has been actively pursued for nearly two decades. One important way to classify these systems is on their implementation. This lumps systems into two basic categories: those that utilize commercial solid modeling kernels and efforts based on proprietary code to represent solid models. Examples of the latter include OYSTER [24], 3DTOP [25], and MemCel [26]. Efforts using commercial solid modeling kernels include VIP3D [27] and MemBuilder [28] (the current mechanism used to build geometry in the commercial system MEMCAD [4]). Geodesic falls into the first category.

Another important classification of these systems is the underlying representation used to represent the geometry. Geodesic, for example, relies on polyhedral representations of geometry. VIP3D relied on a boundary-representation (bRep) [29], a common model representation used in solid modeling. A bRep solid can contain polygonal faces and a

polyhedra can be directly represented directly in a bRep. The distinguishing characteristic between these two solid model representations, however, is that a bRep includes analytic surfaces such as NURBS and swept surfaces.

### **3.2.3 Surface representation**

An important design decision in Geodesic was to use polyhedra instead of analytic surfaces such as NURBS. The motivation for this was twofold. First, boolean operations on analytic surfaces can be problematic, particularly on the types of surfaces generated by the techniques discussed later. Second, all of the process simulators used in this work required discretized geometry. This would require a translation of the simulation results from polyhedra into more complex analytic representations which can be difficult.

### **3.2.4 Process emulation vs. process simulation**

Often for complicated structures, or depending on the versatility of the processing steps allowed in the package, non-physical process steps must be introduced to be able to create geometry that mimics what is expected. For example, a common processing step in the fabrication of micro-devices is conformal deposition. However, if your geometry engine cannot perform a conformal deposition, you can sometimes emulate this process using deposition, planarization, and etching with additional masks. Two of the examples discussed in section 3.3 highlight the differences between process emulation and simulation. The reactive ion etching example shows that the results of emulation can be implementation specific, while the level set example shows the inability to properly capture rounded corners and the results of select etches using emulation.

### **3.2.5 Accessibility to algorithms which achieve multiple levels of physical accuracy**

Since devices and desired levels of simulation accuracy vary significantly, Geodesic was designed as an integrated environment to permit varying degrees of physical accuracy. It is important, particularly from a designer perspective, to have a single tool capable of generating geometry from the earliest conceptual stage to final production when detailed knowledge of the fabrication processes can be tweaked for higher yield or better reliability. In addition to an efficient and robust method to create geometry using only solid modeling operations, Geodesic provides the capability to smoothly incorporate physically based 2-D and 3-D deposition and etching process simulation results into the geometry. Three key approaches are employed to achieve varying degrees of physical accuracy: a geometric-based deposition algorithm, domain decomposition, and level set process simulation (see 3.1.4.3).

First, an efficient geometric-based deposition algorithm (detailed in [30]) and standard solid modeling operations form the basis of the process emulation capabilities inside of Geodesic. The algorithm provides for surface angle dependent deposition thickness to allow for non-uniform sidewall and step coverage. The algorithm was designed to be independent of the solid modeling kernel used. Additional details can be found in section 3.4. Second, a domain decomposition algorithm (detailed in [31]) was created to improve the overall computational efficiency for building complex geometries for devices requiring process simulation. The device is decomposed (using the etch masks) at each deposition or etching step into regions identified as needing 1-D, 2-D, or 3-D process simulation. Different geometric and physical approaches to

geometry manipulation can be arbitrarily applied among these regions. The domain decomposition algorithm is a critical enabling technology for the level set technique because it drastically reduces the processing power and memory requirements needed to perform process simulation for a realistic size micro-mechanical device. Finally, Geodesic contains a fully integrated general multi-dimensional level set kernel (detailed in [32]) which can be used for process simulation (see also section 3.1.4.3).

### **3.3 Examples**

#### **3.3.1 Overview**

Four examples are included in the results section to highlight the versatility and power of the Geodesic framework:

1. Process emulation
2. Extending geodesic
3. Level set process simulation
4. Internet prototyping

First, the canonical rf switch example gives a detailed look at using the CCPDS specification to generate the geometry of a device fabricated using the MUMPS process. The table shows for each processing step the command specified, the resulting geometry, and implementation issues for the given step inside of Geodesic. Several other examples of the same nature are included with the CD-ROM.

The second example highlights the flexibility and extensibility of the Geodesic framework. Although the default geometric etching algorithm is implemented as described in [11], it may be desired to more accurately account for the effects of anisotropic etching. This example highlights one way of implementing process emulation of reactive ion-etching. Many extensions such as this one are possible because process emulation routines are implemented at a script level using lower level primitives in Geodesic.

The third example shows off the capabilities of the 3-D level set kernel. An example of conformal deposition and selective wet etching shows the geometric features that can be captured using process simulation instead of emulation.

Finally, the efforts in internet prototyping are summarized. It is shown that using a standard web-browser with an internet connection geometry of practical interest can be generated on a remote server and displayed on a local machine.

#### **3.3.2 Example of creating the canonical RF switch test device**

As part of this contract an extensive analysis was performed of a canonical RF switch test structure (see [33] for details). Fig. 3-5 shows the schematic of the device and several SEMS of the device which was fabricated using the MUMPS process:

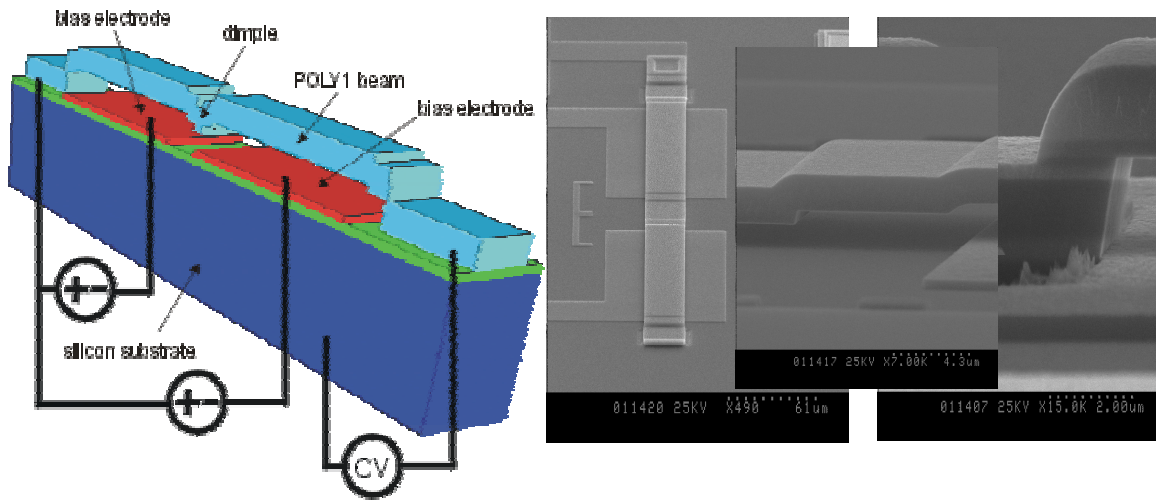


Figure 3-5: Schematic of canonical RF switch and three different SEM views.

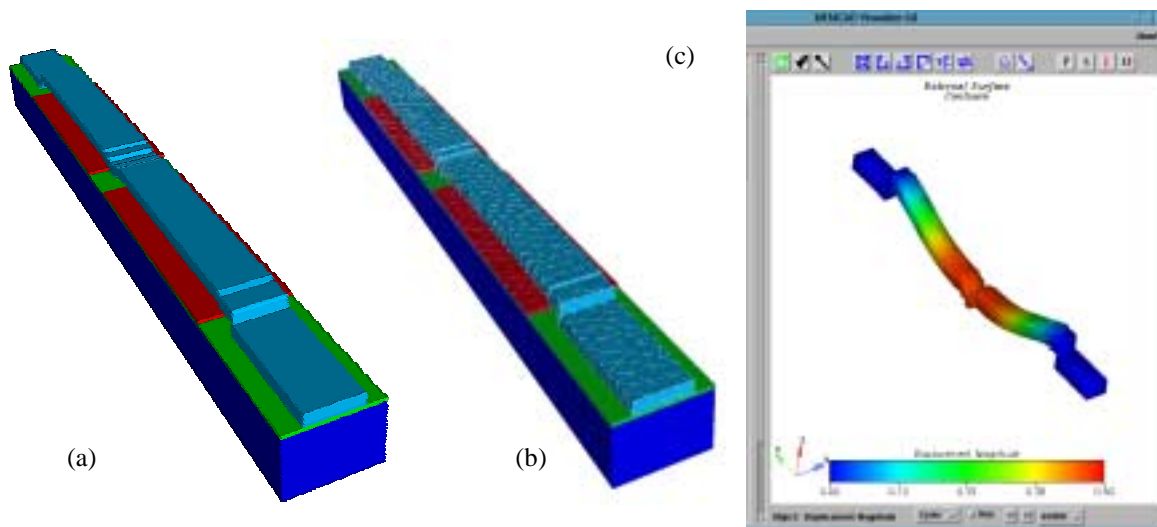


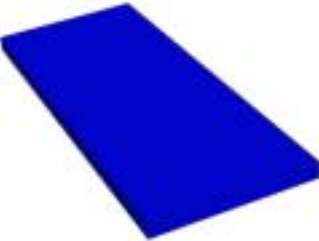
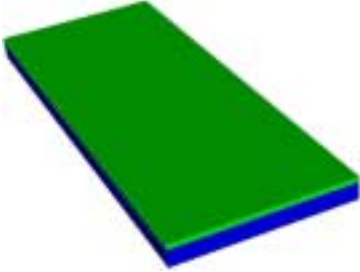
Figure 3-6: Model created using process simulation (a) and meshed (b) in Geodesic and then simulated using MEMCAD (c).

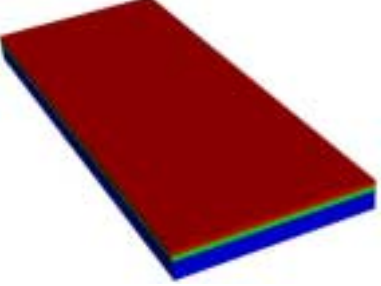
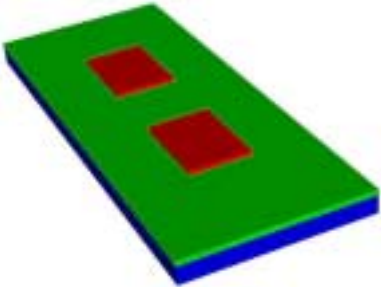
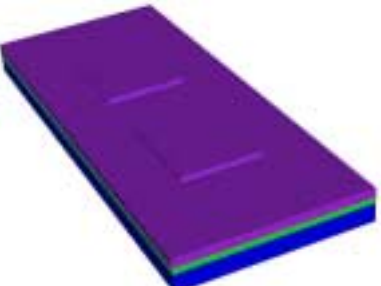
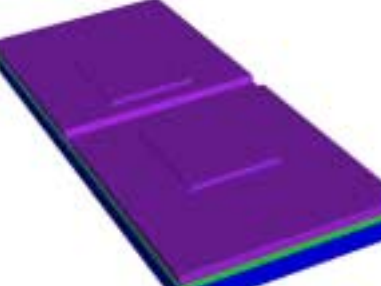
Experimental investigation determined that the sidewalls of the device were not vertical, and that the undercut was occurring during several of the etching processing steps. In addition, simulation results contained in [33] determined that properly capturing these processing effects were critical in calculating the performance of the device. A CCPDS process flow for MUMPS

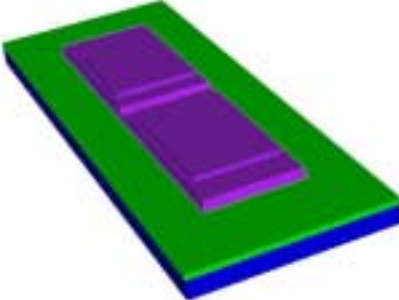
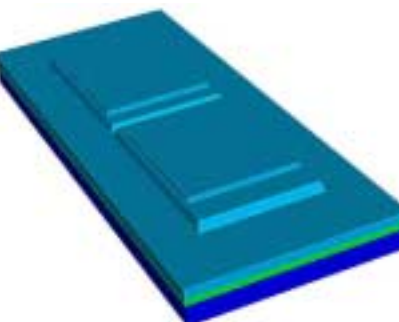
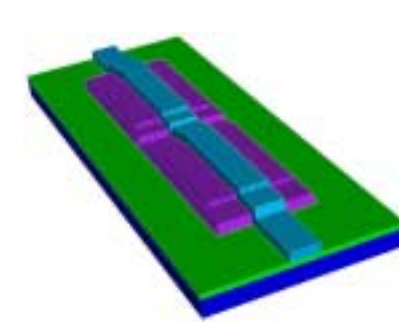
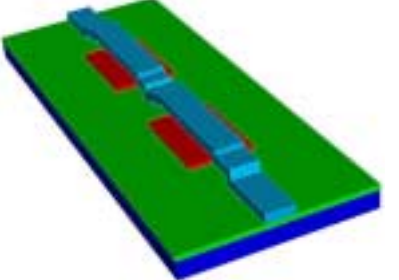
(similar to that found in [11]) detailed below demonstrates how to build a 3-D solid model representing the switch for electro-mechanical simulation. Fig. 3-6 shows the device created in this example meshed and passed to MEMCAD for electro-mechanical simulation.

Table 3-1 below shows the processing commands used in conjunction with the CIF file found in Fig. 3-7 to create the geometry of the RF switch.

Table 3-1: 12 steps in the process flow for the canonical RF switch. The left column shows the CCPDS command for the given step. The middle column shows the geometry resulting from the given command while the right column discusses important implementation details (*italics* are used for variables while **bold** text is used for actual procedure names found in Geodesic [34]).

step	CCPDS command	Geometry after Command	Comments
1	ProcessVersion={ Version="1.0" }		This command specifies the version number of the CCPDS file.
2	ProcessUnit={ Unit=microns }		This specifies the units to be used throughout the model creation process.
3	Wafer={ MaskName="GND" Thickness=10 Color=blue CIF_filename=masks.cif Lambda=1 }		Creates a 3-d rectangular solid of <i>thickness</i> representing the wafer. It is oriented such that the bottom is in the plane $z=0$ . The <i>maskName</i> mask consists of a single CIF box which specifies the center, length, and width of the region of interest.
4	Deposit={ DepositType=CONFORMAL Face=TOP LayerName="Nitride" Thickness=0.6 Scf=c Color=green }		Since the device is still planar (no etches have been performed), the deposit routine calls <b>vfabGeometricDeposit</b> which creates a rectangular solid of thickness properly oriented in space (with layer <i>centroid</i> = $overall\_height + (thickness / 2)$ ).

5	<pre>Deposit={ DepositType=CONFORMAL Face=TOP LayerName="Poly0" Thickness=0.5 Scf=c Color=red }</pre>		<p>This deposit is done the same way as step 4. All conformal depositions are performed this way until an etch is performed. Once an etch is performed, <i>device_is_planar</i> is set to FALSE for the rest of the steps (unless a MechanicalPolish or DepositType=FILL is performed).</p>
6	<pre>Etch={ EtchType=SURFACE Face=TOP MaskName="CPZ" EtchMask=OUTSIDE Depth=3 Angle=87 Undercut=0.157 EtchRemoves="Poly0" }</pre>		<p>This etch step causes the variable <i>device_is_planar</i> to be set to FALSE. Since this etch involves an undercut and results in angled sidewalls, <b>vfabAngledEtch</b> is used. Only the <i>Poly0</i> layer is effected by the etch since it appears within the EtchRemoves.</p>
7	<pre>Deposit={ DepositType=CONFORMAL Face=TOP LayerName="ox1" Thickness=2 Scf=.01 Color=purple }</pre>		<p>Since <i>device_is_planar</i> is FALSE, we have to use the more general <b>vfabOffsetDeposit</b> algorithm which in essence creates the deposited layer by offsetting the original geometry by <i>thickness</i> along the surface normals.</p>
8	<pre>Etch={ EtchType=SURFACE Face=TOP MaskName="DIMP" EtchMask=INSIDE Depth=1.2 Angle=75 Undercut=0.32 EtchRemoves="ox1" }</pre>		<p>This etch uses <b>vfabAngledEtch</b>. Note that EtchMask=INSIDE tells the geometry engine to remove the material “underneath” the mask layout. In actual fabrication this corresponds to a negative resist.</p>

9	<pre>Etch={   EtchType=SURFACE   Face=TOP   MaskName="MORE"   EtchMask=OUTSIDE   Depth=4   Angle=75   Undercut=0.32   EtchRemoves="ox1" }</pre>		<p>This etch uses <b>vfabAngledEtch</b>. Note that EtchMask=OUTSIDE tells the geometry engine to remove the material from around the mask layout. In actual processing this corresponds to a positive resist.</p>
10	<pre>Deposit={   DepositType=CONFORMAL   Face=TOP   LayerName="Poly1"   Thickness=2   Scf=.01   Color=deepskyblue }</pre>		<p>Again since <i>device_is_planar</i> is FALSE we use the general offset algorithm as in step 7. Note that it is very important that small features that would “fill in” such as dimples be removed from the masks by the user in a layout editor before using the offset solid algorithm. The algorithm does not allow for topologic change (you need to use an algorithm such as the level set method for this).</p>
11	<pre>Etch={   EtchType=SURFACE   Face=TOP   MaskName="TOP"   EtchMask=OUTSIDE   Depth=6   Angle=90   Undercut=0   EtchRemoves="Poly1" }</pre>		<p>Since there is no undercut or angle required by this etch, <b>vfabGeometricEtch</b> is used. This corresponds to simply extruding the mask in the z-direction by <i>depth</i> and subtracting the resulting extruded-solid from the layer (Poly1) specified by the EtchRemoves token.</p>
12	<pre>Etch={   EtchType=SACRIFICIAL   Face=TOP   EtchRemoves="ox1" }</pre>		<p>The sacrificial etch removes an entire layer from the database. No visibility calculations or the like are performed. This means that completely unphysical processes (such as removing unexposed material) can be performed using this command.</p>

```
(CIF file for canonical_3d.ccpds);
DS 1 1 1;
L GND;
B 60 500 0 0;
L DIMP;
B 100 10 0 0;
L MORE;
B 100 360 0 0;
L CPZ;
B 40 150 0 -90;
B 40 150 0 90;
L TOP;
B 30 500 0 0;
DF;
C 1;
E
```

Figure 3-7: CIF file for canonical test device.

### 3.3.3 Example of extending Geodesic – Reactive ion etching

In the current implementation of the CCPDS inside of Geodesic, etching is performed by extruding the mask and subtracting the resulting solid from the layers specified by the “EtchRemoves” option. While this emulates some physical processes well, on non-planar geometry it can be a poor approximation. Fig. 3-8 shows a schematic of reactive ion etching. The yellow region on the left represents the material that should be removed by an idealized reactive ion etch of unit depth. The figure on the right shows what occurs using the “vfab” scripts inside of Geodesic to perform the etch. In this case the yellow region represents material which should have been removed but was not.

One of the examples included with the beta release of Geodesic has an example script implementing an idealized reactive-ion etch. The key points of this example are now summarized. We assume we have three given objects:

1. 3-D solid model of a layer named “etchMe” we wish to etch by a unit depth.
2. 2-D polygonal solid of an etch mask named “myMask”.
3. 3-D solid named “mems\_device” which is the exterior of the entire device.

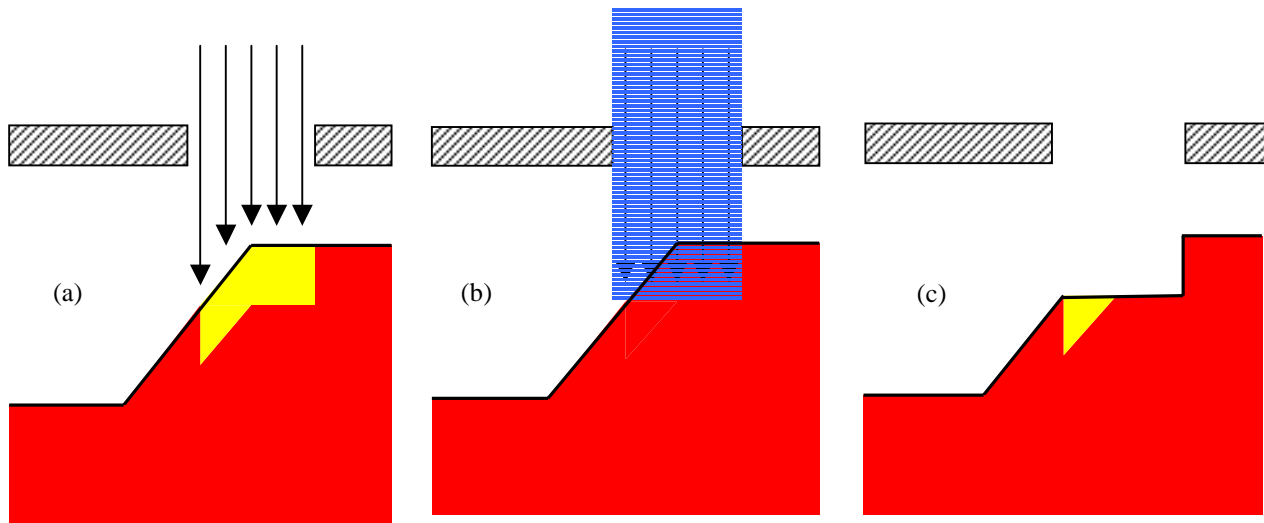


Figure 3-8: The left figure (a) shows in yellow the material which should be removed by an idealized reactive ion etch. The middle figure (b) shows the effective extrusion of the mask by a unit depth, and the right figure (c) shows the material actually removed by the etch simulated using an extruded version of the mask.

A normal idealized etch (Fig. 3-8 b,c) in pseudo-code would be:

```

# extrude the mask in the z-direction by 1 unit
# note: the 2d-solid mask is in the z=0 plane
solid_extrudeZ -src myMask -dst extruded_mask -dist 1.0

# translate the solid of the extruded mask so that it is
# properly oriented in space
extruded_mask Translate -vec {0 0 (overall_height - deposition_thickness)}

# now do a boolean subtraction of the etch mask from the layer to be etched
solid_subtract -result tmp -a etchMe -b extruded_mask

# now replace the existing object with the desired result
solid_copy -src tmp -dst etchMe

```

8b

8c

The reactive ion etch involves more steps (see Fig. 3-9):

```
# the offset solid routine works only with polyhedra, so we extract the facets
# from mems_device:
mems_device GetPolyData -result device_polydata          9a

# note: several Vtk procedures are called at this point to merge coincident points and
# consistently orient the triangles of device_polydata. See the example on the CDROM
# for more details.

# offset the solid for a “negative deposition.” That is, we want to move the surfaces
# inward along the surface normal. Since by convention inside of Geodesic the surface
# normals point inwards, we actually specify a positive displacement.
vfab_OffsetSolid -src device_polydata -dst tmp_polydata -offset 1.0          9b

# the output of the offset solid command is a vtkPolyData object, so now we create
# a solid polyhedra
solid_poly3dSolid -result tmp1 -src tmp_polydata -facet Union          9c

# now we subtract the offset solid from the original solid. This effectively leaves us
# with a solid which could be subtracted from the original geometry to do a unit depth
# ion etch over the entire device. However, we only want to etch the area exposed by
# the mask.

# we now want to find the material which should be removed because it is exposed by
# the mask. To do this, we intersect a solid representing the visible area with “tmp1”.
solid_extrudeZ -src myMask -dst tmp2 -dist overall_height          9d
solid_intersect -result tmp3 -a tmp1 -b tmp2          9e

# now do a boolean subtraction of the etch mask from the layer to be etched
solid_subtract -result tmp4 -a etchMe -b tmp3          9f

# now replace the existing object with the desired result
solid_copy -src tmp4 -dst etchMe
```

We have then emulated a reactive ion etch as desired, with a resulting geometry pictured in Fig. 3-9f.

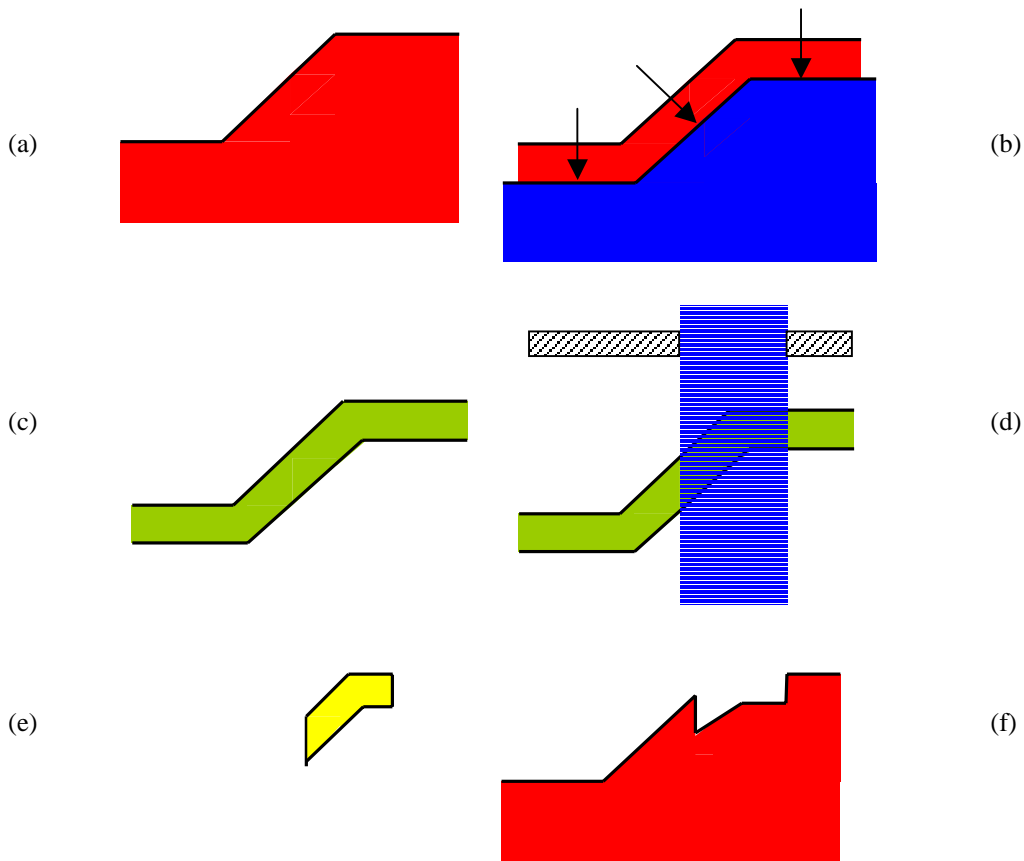


Figure 3-9: Schematic of the 4 step process to emulate a reactive ion etch. (a) shows the original geometry, while (b) shows the offset of the top surface in the direction of the inward normal. (c) shows the result of the Boolean subtraction of the solid created in (b) from the original solid in (a). This layer would correspond to a reactive-ion etch over the entire surface. (d) shows the intersection of rectangular solids created based on the etch mask to represent the area of the wafer exposed by the etch mask. Finally, the resulting solid from (d) shown in (e) is subtracted from (a) to obtain the desired result.

### 3.3.5 Example using Geodesic level set module: Process simulation

The use of process emulation, and in particular solid modeling based methods to build geometry such as the CCPDS, works for many cases of interest. However, there are practical situations where topologic change can occur (e.g. via or dimple filling) and the “boxy” nature of the methods created using the CCPDS standard are insufficient. In these cases one must utilize more sophisticated techniques to create the desired geometry. One such method is the level set method. There is a rich body of literature on using the level set method with appropriate velocity functions to simulate IC processing steps such as deposition and etching [20].

The level set equation of evolution is:

$$\Phi_t + V |\nabla\Phi| = 0$$

where:  $\Phi$  = scalar function implicitly representing interface (locus where  $\Phi=0$ )  
 $V$  = velocity function normal to the propagating interface incorporating physics of deposition/etching

In this example we utilize the level set kernel inside of Geodesic (detailed in [32]) with two velocity functions to simulate wet etching and conformal deposition. In the case of conformal deposition, we assume a constant normal velocity  $v = 1.0$ . In the case of etching we assume a velocity function which simulates selective isotropic etching.

Inside of Geodesic, the setup required to simulate conformal deposition and isotropic selective etching is very similar. In the case of deposition, we track the top surface of the device using the scalar field  $\Phi$ . In etching, on the other hand, we actually track the boundary of the “air” region surrounding the device (i.e. the scalar field  $\Phi$  implicitly represents the surface of the air region). The reasoning behind the difference is simple. We are only using the zero level set ( $\Phi = 0$ ) to define a material interface, so we can represent only one material with  $\Phi$ . Since we want the ability to do selective etches on multiple materials, we represent the boundary of the “air” region. In the case of isotropic wet etching, this can be thought of physically as tracking the surface of the etchant.

The following pseudo code highlights the important aspects of performing process simulation inside of Geodesic using the level set kernel (the actual scripts are included in the examples with the software distribution):

```
# define the desired deposition thickness / etch depth
thickness = 1.0

# create a solid with a raised center block in the center
solid_box3d -result box1 -dims {...} -ctr {...}
solid_box3d -result box2 -dims {...} -ctr {...}
solid_union -result input_geom -a box1 -b box2

# create air region
solid_box3d -result tmpair -dims {...} -ctr {...}
solid_subtract -result air -a tmpair -b input_geom

# Set up grid domain
h = {0.500 0.500 0.500}
origin = ... (lower left hand corner of solution domain)
```

```

dims = ... (overall extent of simulation domain)

# Instantiate velocity function
# deposition == constant function (setVConst)
# etch == selective etch function (lsetVSELetch)

if (deposit) {
    velocity = 1.0
    setVConst vfn
    vfn SetV -v $velocity
}

if (etch) {
    lsetVSELetch vfn
    vfn SetRate -rate 1.0
    vfn AddRegion -obj box2 -sel 0.1
    vfn AddRegion -obj box1 -sel 1.0
}

# Compute time-step parameters to give desired deposition thickness.
# The level set kernel automatically calculates the maximum allowable time step
# based on the CFL condition. In this case, since V = constant, we can directly
# calculate the number of times steps the kernel needs to perform to deposit
# the desired amount of material.
numSteps = ...

# Setup level set core

lsetCore core

core SetTime -simTime -1.0 -cflFactor 1.0
core SetGrid -h $h -dim $dims -origin $origin \
    -type SparseGrid -bandExt {...}
core SetVelocity -vobj vfn
core SetTimers -flag 0

# initialize based on desired process to simulate
if (deposit) {
    core SetSolidSeed -solid input_geom
}

if (etch) {
    core SetSolidSeed -solid air
}

```

```

core Init

# the "lset_for" loop runs the level set simulations for a given number of time
# steps.
set verbose 0
lset_for core $numSteps { } $verbose 1 0

# extract a surface, which either represents the top surface of the new
# material in a deposition or the surface of the "air" region in the case of an
# etch.
core ExtractFront -out output_pd -closed 0

```

Fig. 3-10 shows the results of the deposition on a corner, while Fig. 3-11 shows the results of an isotropic etch with materials of two different selectivities.

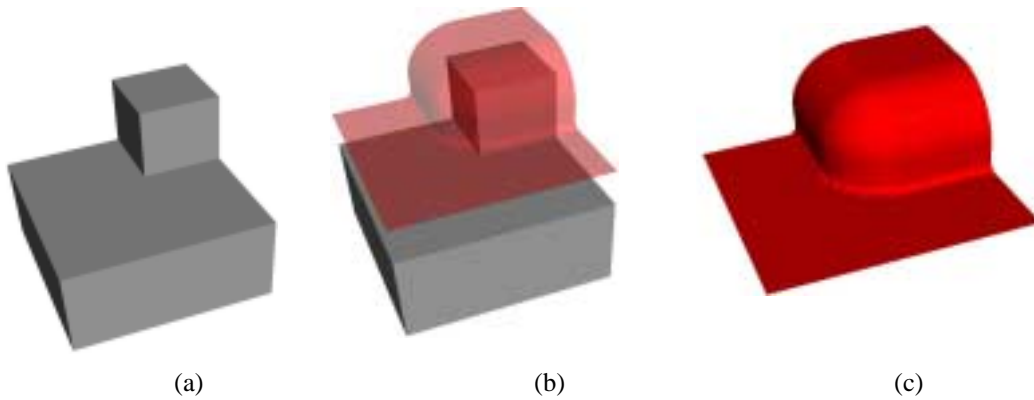


Figure 3-10: A conformal deposition of unit thickness on a corner. (a) original corner, (b) corner with deposition, (c) close up of levelset function.

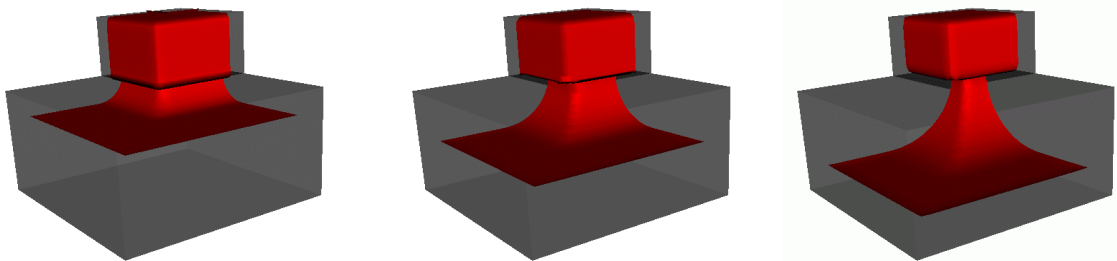


Figure 3-11: Example of a selective corner etch using the integrated 3-D level set kernel in Geodesic. The figure shows three steps in the evolution of the boundary surface, where the red surface indicates the level zero function. As can be seen, the small block on top of the larger block is more resistive to etch.

### 3.3.6 Examples of internet based prototyping

The proposed client-server architecture for MEMS prototyping discussed in section 3.1.3 is demonstrated with several representative device examples. Fig. 3-12 shows a representative mesh of a simple switch and a micromirror. In addition, Fig. 3-13 shows typical electro-mechanical devices such as switches, micromirrors, and combo drives created using the web-based environment (Fig 3-3). Table 3-2 shows examples of file sizes for the various micro-electro-mechanical devices. Both VRML and OOGL (the file format used by JGV) are ASCII file formats. Most VRML browsers permit the input files to be compressed using the gzip compression algorithm. This greatly reduces the size of the actual file transmitted, as can be seen in Table 3-2. As the table indicates, all of these geometries can be transmitted in a reasonable amount of time even over a 56 Kbps modem (i.e. low bandwidth connection). Also shown are example file sizes for coarse meshes for each of the devices. Note that even though a volume mesh is being generated for each device by the server, only the surface mesh needs to be transmitted back to the client for viewing. These results show great promise for internet-based prototyping of microsystems as an area for future work.

Table 3-2: File size (in bytes) of four example MEMS devices.

Device	Geometry		Surface Mesh	
	VRML*	OOGL	VRML*	OOGL
Dual Electrode Switch	6116	43119	9926	61510
Comb Drive	52257	479440	87137	580514
Torsional Micromirror	4215	28743	11827	149934
Simple Switch	1429	8012	2762	30909

\*gzipped file size

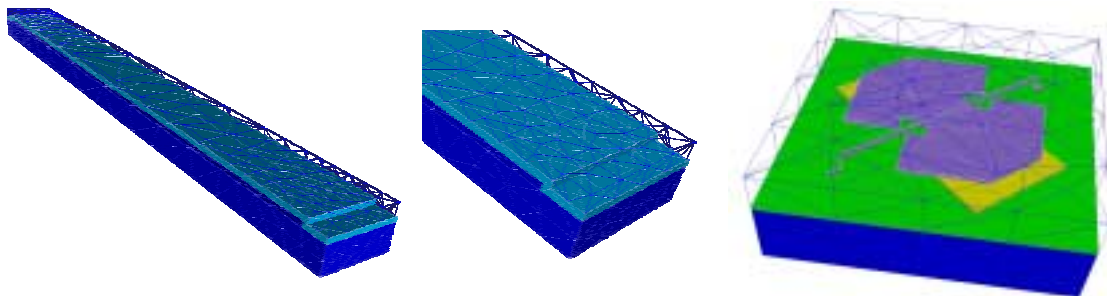


Figure 3-12: Two examples of mesh generation. The simplified switch (a) and the close up of the step up (b) showcase automatic mesh generation with grading. The mesh for the micromirror (c) was also created automatically. Note: All of the meshes are volume meshes with only the exterior surfaces of each layer shown for clarity. In addition, the air region around each device was meshed as indicated.

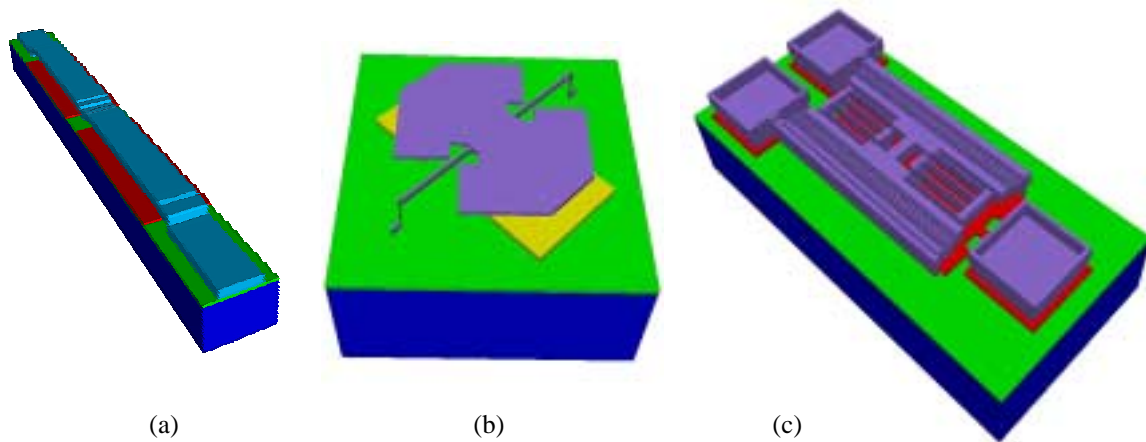


Figure 3-13: Three different MEMS geometries created using Geodesic. The switch (a) was created using domain decomposition and process simulation. The micromirror (b) and comb drive (c) were created using the geometric algorithm. Geometries exaggerated in the z-direction for clarity.

### 3.4 A solid modeler independent implementation of the Composite CAD Process Definition Specification

#### 3.4.1 Introduction

The “Composite CAD Process Definition Specification 1.0” [11] is a proposed standard for MEMS CAD vendors to specify the process flow used to create geometry (i.e. solid models) for simulation. The file format is the product of over a year of interaction of numerous vendors which resulted in a useful format with wide application for microsystems. The standard had several key design objectives. First, it was designed to be an ASCII text file that was “human readable.” In addition, the processing steps were to be the most common used in microsystems (with particular focus on process operations which altered the physical geometry). Finally, version 1.0 was designed to be a minimal standard so that maximum compliance across vendors could be achieved.

This section describes the implementation details of the basic standard found in [11]. Here the overview of a solid modeler independent implementation is given. The actual source code can be found on the CD-ROM. The CCPDS format consists of eight commands, which are organized functionally in Table 3-3:

Table 3-3: CCPDS commands organized by functionality

<b>Book-keeping</b>	<b>Process Emulation</b>	<b>Process Macros</b>	<b>Misc</b>
ProcessVersion ProcessUnit	Deposit Etch Mechanical Polish	ImplantDiffuse Grow	Wafer

Each of the four functional categories will be discussed separately. It should be noted that the “basic” CCPDS requires only solid modeling operations to build geometry of interest. While this standard is useful for many applications, section 3.4.4 will close by discussing the limitations and ambiguity in the file format. An import example outside of the current standard is utilizing process simulation to build geometry was seen in section 3.3.

### **3.4.2 Discussion of commands**

#### **3.4.2.1 Book-keeping**

These commands are not specific to any particular step in the process flow. They typically should appear first in a given process flow since they effect the meaning of the other commands in the file.

1. ProcessVersion

This command allows the user to specify the version number of the process flow file. It is useful since it allows for the standard to evolve in the future without invalidating the users existing process flows. In addition, it permits the vendor to determine if the user has imbedded extra information in the file (e.g. extensions).

2. ProcessUnit

This command allows the user to specify the units to be used in creating the model. All of the operations in the basic standard have been implemented to be dimensionally independent.

#### **3.4.2.2 Miscellaneous**

The only miscellaneous command consists of the “Wafer” command. This is an important command that must appear prior to any processing steps in the process flow. The wafer is specified using a box in the CIF file, and is specified such that the “bottom” of the wafer is in the plane  $z=0$ . All additional processing steps (e.g. depositions) will take place on the wafer. This allows us to define the “overall height” of the device as the distance from the bottom of the wafer to the maximum  $z$ -coordinate in the model.

### 3.4.2.3 Process macros

Process emulation macros differ in a significant way from the other process emulation commands. Namely, while these commands represent common IC processing steps (e.g. dopant implant and diffusion), the implementation proposed in the standard requires significant approximations and consist of performing a fixed sequence of steps using other commands from the CCPDS. For completeness the major steps involved are listed, but the reader is referred to [11] for the detailed explanation of these macros.

#### 1. Grow

This command is a gross approximation to the growth of thermal oxide on a silicon substrate. It does not predict residual stress or other physical characteristics of this processing step. It consists of the following sequence of fundamental steps:

- a. etch silicon that would be converted during the thermal oxidation
- b. deposit oxide
- c. etch oxide where growth would be inhibited by a nitride mask

#### 2. Implant Diffuse

This command allows the user to create multiple solid regions from an initial layer (e.g. to assign differ material properties to a region of higher doping). It consists of the following sequence of fundamental steps:

- a. etch initial layer
- b. deposit layer of higher doping
- c. etch layer of higher doping

### 3.4.2.4 Process emulation

The process emulation commands consist of methods to add material (deposition) and remove material (etch, mechanical polish) from a given wafer. Recall that these are process emulation steps in that the user must know the final outcome of the real processing step (e.g. deposition thickness).

There are three types of emulated deposition supported by the CCPDS standard: conformal, snowfall, and fill. We will further subdivide conformal deposition into two categories for implementation purposes: planar and general-topology. Geodesic has an additional physical deposition type that can be invoked to use process simulation. See the results section (Fig. 3-10, 3-11) for a discussion on process simulation using the level set method. Fig. 3-14 shows the organization of the deposition commands. The only CCPDS deposition type not explicitly permitted is “snowfall.” This can be integrated in a straight forward manner by adding an anisotropic velocity function which takes into account visibility calculations and sticking coefficients (see [20]). Fig. 3-15 shows graphically the conformal and fill deposition types. The conformal deposition on a non-planar topology relies heavily on the offset solid algorithm detailed in [30].

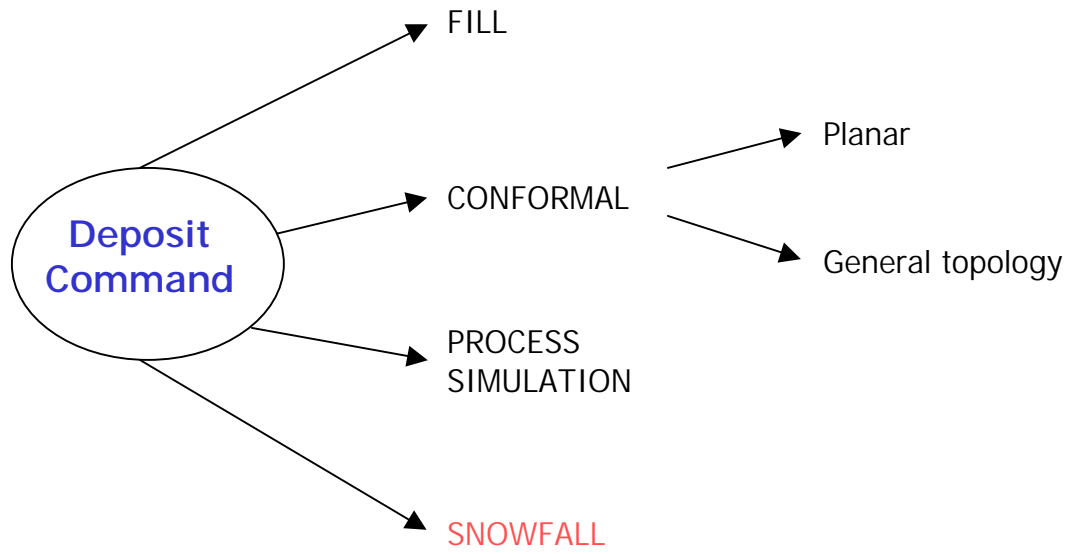


Figure 3-14: Deposit types flow chart.

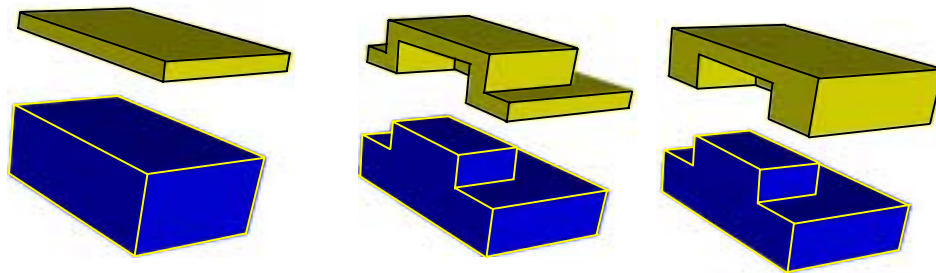


Figure 3-15: Three types of deposition. (a) shows planar deposition, (b) shows conformal deposition, and (c) shows a fill operation.

Fig. 3-16 shows schematically the steps involved in using the offset solid algorithm to perform a conformal deposition. In a preliminary step, all of the current layers and wafer for the device are unioned together simplifying all internal boundaries. This leaves a solid with only exterior walls (i.e. free surfaces) as seen in Fig 3-16 (a). Conceptually, we want to generate a new solid (d) that we can subtract the original geometry (a) from and have the result be the deposited material. This requires four major steps. First, the bottom and sides of the wafer are identified (b) and fixed so they cannot move. This can be thought of as only wanting to deposit material on top of the wafer. Second, infinite planes representing the remaining faces are offset in the direction of the normal by the specified deposition thickness (this can be a function of the normal direction). Third, the vertices of the model are cycled over. At each vertex, the intersection of all infinite planes representing the faces meeting at the vertex is calculated. Assuming the topology of the device doesn't change, these vertices along with the original connectivity define the new geometry shown in (d). The final step consists of doing a boolean subtracting of (a) from (d) to get the desired result.

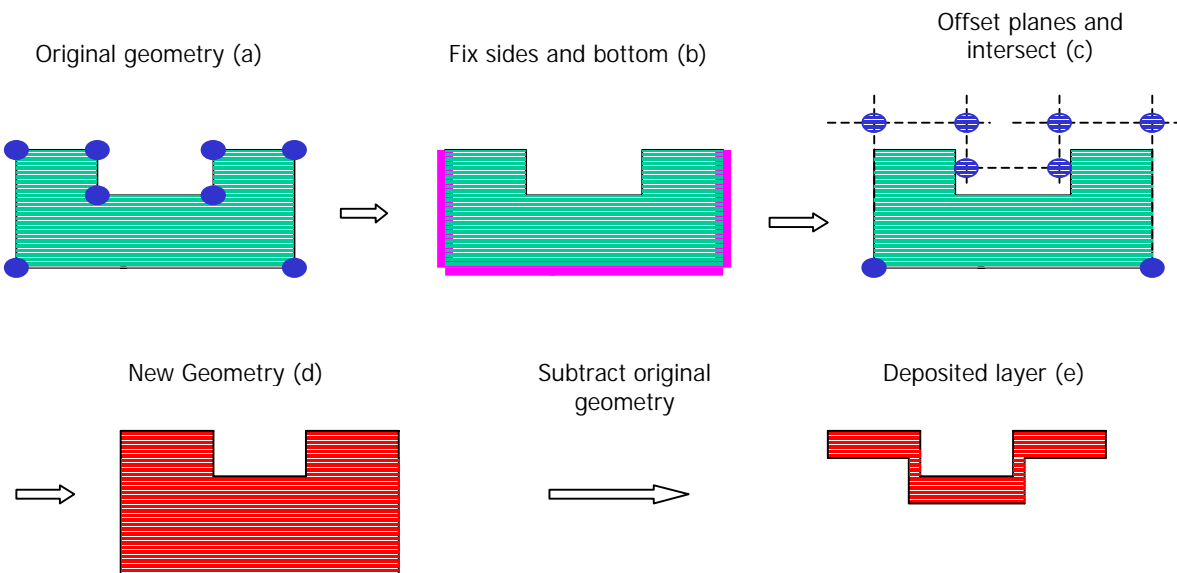


Figure 3-16: Using the offset solid algorithm in Geodesic to generate a conformal deposition. Conceptually, we want to generate a new solid (d) that we can subtract the original geometry (a) from and have the result be the deposited material.

There are three types of etching defined in the CCPDS: Sacrificial, Surface, and Bulk. In addition, Geodesic has an additional type of etching using the level set kernel for physical process simulation. For implementation purposes, we further subdivide surface etching into two categories: ideal, and undercut with angled-sidewalls. The standard also subdivides surface etching into two types: inside and outside. Fig. 3-17 shows the organization of the etch commands.

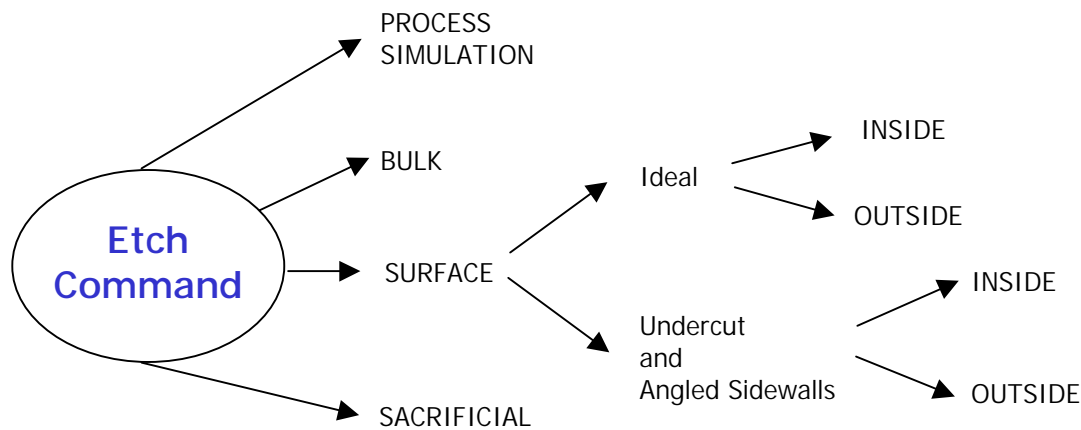


Figure 3-17: Etch types flow chart.

The sacrificial etch represents the release step commonly used in microsystems. In the present implementation, this corresponds to deleting the specified layer of material. This is an approximation that assumes that the material is ideally (i.e. completely) removed, and that the entire sacrificial layer is exposed to etchant. This is not always the case, and special procedures will have to be employed if part of the sacrificial material is to be maintained in the final device geometry.

The case of surface etching with vertical sidewalls and no undercut begins with extruding the mask in the z-direction by appropriate depth of the etch. If “EtchMask=INSIDE” is specified, then this extruded solid is subtracted from each layer specified in the command step. If “EtchMask=OUTSIDE” is specified, then a two step process is required. The first step involves creating a “negative” of the extruded mask solid by subtracting the extruded mask from a rectangular solid the size of the wafer with a thickness of the etch depth. The second step involves subtracting the negative mask solid from each layer specified in the command step.

Performing a surface etch with angled sidewalls and / or undercut is more complicated. The masks are required to consist of non-overlapping simple CIF box objects. The box is then scaled by the undercut value depending on the type of etch performed. Outside etches require the box edges move inward by the specified undercut, while an inside etch requires the box edges move in the outward direction by the specified undercut. Using trigonometry, the image of the box is also calculated at the specified depth of the etch. The end result is eight vertices with a known connectivity which can be used to create a trapezoidal solid. The aggregation of these trapezoidal solids is then used in place of the extruded etch mask, and the process of handling the “EtchMask=INSIDE” and “EtchMask=OUTSIDE” is identical to the vertical wall case. Note that only simple etch masks are handled properly with this implementation. Overcoming this

limitation likely requires performing identical operations as discussed on arbitrary polygonal shapes.

The final type of etching in CCPDS is anisotropic bulk etching (i.e. EtchType=BULK). The bulk etching option is a special case of surface etching with angled sidewalls. The first step is to find the minimum bounding box (MBB) of the specified etch mask. Using the resulting MBB as a pseudo mask, a surface etch with a sidewall angle of 54.7 degrees is then performed.

### **3.4.3 Additional notes on implementation of CCPDS inside of Geodesic**

There is a general description of the Geodesic architecture in section 3.1.4 of this report, and it is important to point out additional key aspects relating to the processing of the CCPDS file to create a solid model. In Geodesic, we utilize the scripting language Tcl to process the CCPDS file (which is typically only a few hundred lines of text) while coding the computational intensive commands in C++ with bound Tcl-interpreter commands. The scripts were written in a modeler independent way by using Tcl-bound commands which have modeler implementations “hidden” from the interpreter level. The user can toggle between solid modelers using the “solid\_setKernel” command (see [34]), and the scripts remain unaltered. Although we have implemented a more general set of solid modeling commands in our modeler-independent API, Table 3-4 indicates the commands required to implement the basic CCPDS standard. In addition to the “solid\_” commands which typically create objects, a SolidModel object has a set of useful methods. Geodesic provides more methods than required to implement the basic CCPDS standard, so Table 3-5 summarizes only the required SolidModel methods to implement the standard.

### **3.4.4 Limitations of the CCPDS standard**

The CCPDS standard has several important limitations. First, it was designed to be a standard that could be implemented using only solid modeling operations as detailed above. However, it is impossible to include the results of detailed process simulation into the final geometry. Second, the standard is predominately written from a 2-D perspective. For example, in surface etching the angle is not clearly defined in the general 3-D setting. Third, it is possible to perform a sequence of depositions and etches which make specifying subsequent steps impossible using just variables such as undercut and angle. Finally, several of the commands are overly simplistic. For example, a sacrificial etch just removes a layer from the model, which can lead to unphysical results if part of the sacrificial layer was not accessible to the etchant.

Table 3-4: Solid modeling commands required to generate geometry\*.

	<b>General</b>	<b>Create</b>	<b>Booleans</b>
<b>Basic CCPDS</b>	solid_getKernel solid_setKernel solid_readNative	solid_box2d solid_box3d solid_copy solid_extrudeZ solid_poly3dSolid solid_polyPts	solid_subtract solid_union
<b>Domain Decomposition</b>	<i>no additional</i>	solid_poly3dSurface solid_extrude	solid_intersect
<b>Level Set</b>	<i>no additional</i>	<i>no additional</i>	<i>no additional</i>

\*Note that only the first six rows are required for generating geometry for the standard CCPDS, while additional commands are required if domain decomposition or level set simulation is desired.

Table 3-5: Solid model object methods required for model generation

	<b>General</b>	<b>Transforms</b>	<b>Classifications</b>	<b>Labels*</b>
<b>Basic CCPDS</b>	GetClassName GetKernel GetPolyData WriteNative	Translate	<i>none</i>	ClearLabel GetLabel GetLabelKeys SetLabel
<b>Domain Decomposition</b>	<i>no additional</i>	Rotate Scale	Find Centroid	<i>no additional</i>
<b>Level Set</b>	<i>no additional</i>	<i>no additional</i>	ClassifyPt Distance	<i>no additional</i>

\*although methods to manipulate labels appear in the solid model object, these are equivalent to the more general “repos\_\*Label\*” repository label commands.

### 3.4.5 Summary of CCPDS

In summary, the CCPDS is an extremely useful file format for specifying process flows relevant for MEMS simulation. Although it has some limitations, these can be overcome by providing extensions and clarifications to the basic standard. Unfortunately, the standard has failed to receive widespread adoption by the commercial MEMS CAD vendors, which limits its ultimate practical effectiveness.

### 3.5 References

- [1] *EE Times*, April 17, 1998.
- [2] E. Peeters, "Challenges in Commercializing MEMS," in *IEEE Computational Science & Eng.*, pp. 44-47, Jan.-Mar., 1997.
- [3] S. D. Senturia, N. Aluru, and J. White, "Simulating the Behavior of MEMS Devices: Computational Methods and Needs," *IEEE Computational Science & Engineering*, Jan-Mar 1997, pp. 30-43.
- [4] S. D. Senturia, R. M. Harris, B. P. Johnson, S. Kim, K. N. Nabors, M. A. Shulman, and J. K. White, "A Computer-Aided Design System for Microelectromechanical Systems (MEMCAD)," in *Journal of Microelectromechanical systems*, vol. 1., no. 1, March 1992. See also <http://www.memcad.com>.
- [5] IntelliCAD, IntelliSense Corporation, 16 Upton Dr., Wilmington, MA 01887, USA. See also <http://www.intellisense.com>.
- [6] J. Funk, "Modeling and Simulation of IMEMS," D. Sc. Techn. Thesis, Swiss Federal Institute of Technology, Zurich, 1995. See also Solidis at <http://www.ise.com>.
- [7] P. Ljung, "Efficient MEMS CAD Tools," *Journal of Micromachining*, June 1998. See also <http://www.coyotesystems.com>.
- [8] CFD Research Corporation, 215 Wynn Drive, Huntsville, AL 35805, USA. See also <http://www.cfdrc.com>.
- [9] J.P. McVittie, J. C. Rey, L.-Y. Cheng, A. Bariya, S. Ravi and K. C. Saraswat, "SPEEDIE: A Profile Simulator for Etching and Deposition," Extended Abstracts, SRC Techcon '90, San Jose, October 1990, pp. 16-19.
- [10] Private communication with designer at Maxim Integrated Products, Inc., 120 San Gabriel Drive, Sunnyvale, CA 94086, USA.
- [11] "Composite CAD Process Definition Specification version 1.0," DARPA internal document.
- [12] "the VRML repository," <http://www.web3d.org/vrml/spv2.htm>.
- [13] "Extensible 3D (X3D) Task Group," <http://www.web3d.org/x3d.html>.
- [14] "JGV: 3D Viewing in Java," <http://www.geom.umn.edu/java/JGV/>.
- [15] Altair Engineering, Inc., 7800 Shoal Creek Blvd, Suite 290E, Austin, TX 78757-1024, USA. See also <http://www.comco.com>.
- [16] Shapes by XOX, Inc., St. Paul MN, USA. See also <http://www.xox.com>.
- [17] Parasolid by Unigraphics Solutions Inc., <http://www.unigraphics.com>.
- [18] IRIT by Gershon Elber, Department of Computer Science, Technion, Israel Institute of Technology, Haifa, 32000, Israel. See also <http://www.cs.technion.ac.il/~irit>.
- [19] ACIS by Spatial Technology, 2425 55th Street, Suite 100 Boulder, Colorado 80301-5704, USA. See also <http://www.spatial.com>.
- [20] J.A. Sethian, D. Adalsteinsson, "An overview of level set methods for etching, deposition, and lithography development," *IEEE Trans Semiconductor Manufacturing*, 10(1), 1997, pp. 167-184.
- [21] M. S. Shephard, "Meshing Environment for Geometry-based Analysis," to appear in *Int. J. Num. Meth. in Engr.*, see also <http://scorec.rpi.edu>
- [22] N. M. Wilson, P. M. Pinsky, and R. W. Dutton, "Investigation of Tetrahedral Automatic Mesh Generation for Finite Element Simulation of Micro-Electro-Mechanical Switches",

- Proceedings of Modeling and Simulation of Microsystems, April 19-21, 1999, pp. 305-308.
- [23] R. W. Dutton, Z. Yu, "Technology CAD - Computer Simulation of IC Processes and Devices," Kluwer Academic Publishers, 1993.
  - [24] G. M. Koppelman, "OYSTER, a three-dimensional structural simulator for microelectromechanical design," *Sensors and Actuators*, vol. 20, 1989, pp. 179-185.
  - [25] J. P. Elliott, G. A. Allan, A. J. Walton, "The Automatic Generation of Conformal 3D Data for Interconnect Capacitance Simulation," *Proc. ESSDERC*, 1995, pp. 405-408.
  - [26] M. Emmenegger, J. G. Korvink, H. Baltes, "MemCel – An Inexpensive and Efficient Tool for 3D MEMS Prototyping," *IMECE*, Anaheim, Nov. 15-20, 1998, pp. 559-563.
  - [27] K. Wang, H. S. Park, Z. Yu., R. W. Dutton, "3D Solid Modeling of IC Structures Using Simulated Surface Topography," *proc. SISPAD*, Tokyo, 1996, pp. 131-132.
  - [28] P. M. Osterberg, S. D. Senturia, "MemBuilder: An Automated 3D Solid Model Construction Program for Microelectromechanical Structures," *Proc. TRANSDUCERS-95*, Stockholm, Sweden, June, 1995, Vol. 2, pp. 21-24.
  - [29] M. Mantyla, *An introduction to Solid Modeling*, Computer Science Press, Rockville, Maryland, 1988.
  - [30] N. M. Wilson, K. Wang, D. Yergeau, and R. W. Dutton, "GEODESIC: A New and Extensible Geometry Tool and Framework with Application to MEMS," *Proceedings of Modeling and Simulation of Microsystems*, March 27-29, 2000, pp. 716-719.
  - [31] N. M. Wilson, S. Liang, P. M. Pinsky, R. W. Dutton, "A Novel Method to Utilize Existing TCAD Tools to Build Accurate Geometry Required for MEMS Simulation," *Proceedings of Modeling and Simulation of Microsystems*, April 19-21, 1999, pp. 120-123.
  - [32] K. Wang, "Level Set Methods for Computational Prototyping with Application to Hemodynamic Modeling," *Stanford University PhD thesis*, expected 2001.
  - [33] E. K. Chan, *Modeling and Simulation of Electrostatically Actuated Micromechanical Devices*, *Stanford University PhD thesis*, 1999.
  - [34] <http://www-tcad.stanford.edu/~mems/geodesic/docs.html>

## 4. Characterization of MEMS Materials Models

**Authors: Dr. Guido Cornella, Dr. Hoo-Jeong Lee, Ping Zhang, Prof. John C. Bravman**

### 4.1 Monotonic and Cyclic Testing of Thin Film Materials for RF Switch Application

In MEMS devices, many of the active components exist in the form of free-standing thin films. Such components are constantly in motion under various actuation or stimulation. Understanding the mechanical properties and modeling the mechanical behavior of free-standing thin films is therefore important for the design of MEMS devices, as well as for predicting their mechanical performance and reliability.

The mechanical behavior of a free-standing thin film is expected to be different from that of bulk material or a conventional thin film on a substrate. In a free-standing thin film, the grain size is typically very small and the absence of a substrate leads to both its top and bottom surfaces being unconstrained. These microstructural characteristics may result in unique mechanical properties. Although thin films on substrates have been extensively studied, knowledge of free-standing thin films was not available until the advent of micromachining techniques and is yet to be further explored. We have developed a sample fabrication process which batch produces free-standing thin film samples using micromachining techniques within a cleanroom facility.

Basic materials parameters that are required for mechanical device modeling are, among others, the stress-strain response for monotonic and cyclic loading. We have built a custom-designed micromechanical testing system that is capable of providing accurate stress-strain data for monotonic loading as well as for cyclic loading up to a very large numbers of cycles. In conjunction with a dedicated sample fabrication process, we are able to carry out mechanical testing on a wide range of free-standing thin films of different materials and different geometry. We use Transmission Electron Microscopy (TEM) to reveal the microstructural features of the samples both before and after testing, which facilitates our understanding of the mechanical properties of the thin film materials under investigation.

One particular MEMS application we are trying to simulate through our testing is the operation of an RF switch. We are interested in its one-time switching behavior as well as its cyclic operation in the kHz frequency range, which correspond to monotonic and cyclic loading conditions, respectively. We are also interested in the stress relaxation behavior, important for when the switch is held at the “on” position for an extended amount of time. We have studied pure Al and Al/Ti-alloyed thin film samples and obtained stress-strain responses as well as stress relaxation data from both monotonic and cyclic loading, and have simulated the stress relaxation behavior by anelastic models.

#### 4.1.1 Sample Fabrication

Specimens were fabricated using micromachining techniques at the Stanford Nanofabrication Facility (SNF). The fabrication process makes use of two masks. The front-side mask defines the micro beams; the backside mask defines the silicon windows to be etched away to release the

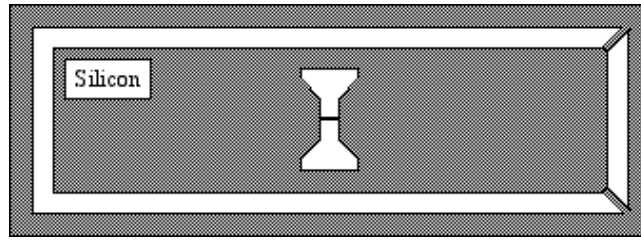


Figure 4-1: Die schematic of a micro beam specimen.

beams. There are 34 dice per wafer, with each die (Fig. 4-1) measuring 8mm×21mm. Each die contains one micro beam (Fig. 4-2), which measures 50μm wide and 500μm long (gauge section), while the thickness varies. For ease of die removal upon completion of the process, a groove about 500μm wide is designed to surround each die. The groove is formed during the silicon backside etch, which leaves the die attached to the remainder of the wafer by only two small silicon support bridges at two corners of the die.

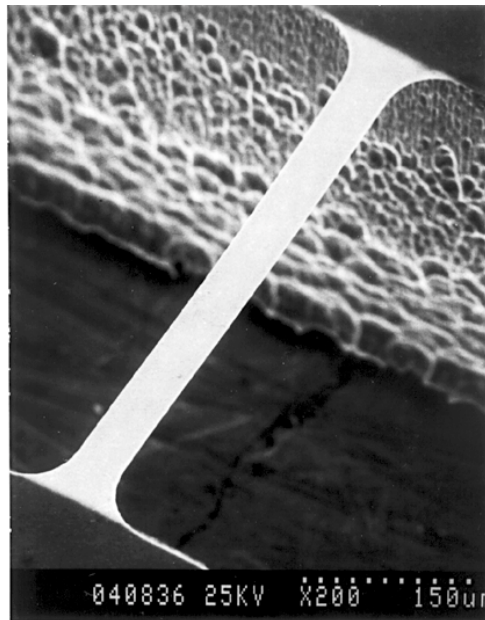


Figure 4-2: SEM micrograph of a free-standing Al micro beam specimen (prior to testing).

We began the fabrication with (100)-oriented 4-inch silicon wafers. First, 1μm of silicon nitride was deposited by Low Pressure Chemical Vapor Deposition (LPCVD) on both sides of the wafer. Using Photo Resist (PR) to protect the front-side nitride, the backside nitride was removed by a dry etch; the front-side nitride was used later as an etch-stop layer during the silicon bulk etch to release the micro beams from the backside. Next, a metal layer (e.g. Al) was sputter deposited onto the front-side of the wafer, and then patterned with the front-side mask to define the micro beams. Afterwards, a thick layer of PR was put down onto the backside of the wafer

and patterned with the backside mask. This patterned PR acted as an etch mask for the removal of silicon from the backside of the wafer through window regions defined by the backside mask. Silicon was then dry-etched through the wafer thickness (about 500 $\mu\text{m}$ ) until the front-side LPCVD nitride was reached. Lastly, the nitride was removed by dry etch from the backside, and the micro beams were released.

For the fabrication of the Al/Ti-alloyed micro beams, we previously employed the method of multi-layer metal deposition. For example, to achieve micro beams of 2% of Ti and 2 $\mu\text{m}$  in thickness, a 7-ply of 0.5 $\mu\text{m}$ -Al/10nm-Ti multi-layer was deposited on the front-side of the wafer during the metal deposition step, followed by subsequent annealing at 550  $^{\circ}\text{C}$  for one hour in a nitrogen atmosphere. We are currently exploring the method of co-sputtering, where metals from the two targets of 100%Al and Al-10%Ti are simultaneously deposited onto the silicon substrate. As we adjust the relative powers of the two targets, ranging from 0.5kW to 8.5kW, we are able to achieve Ti concentrations in the range of 1.5%-5.5%.

## 4.1.2 Experimental Setup and Procedures

### 4.1.2.1 Micromechanical Testing System

The heart of the custom-designed micromechanical testing system (Fig. 4-3) is a custom-designed piezo-actuator-driven test rig with a load resolution of  $\pm 0.2\text{mN}$  and a displacement resolution of  $\pm 10\text{nm}$ . It comprises a piezoelectric actuator with position sensor, a load cell with temperature sensor, a height-adjustable alignment stage, and sample grips that are attached to the piezo-actuator and load cell. The control electronics include a waveform generator, an amplifier, a

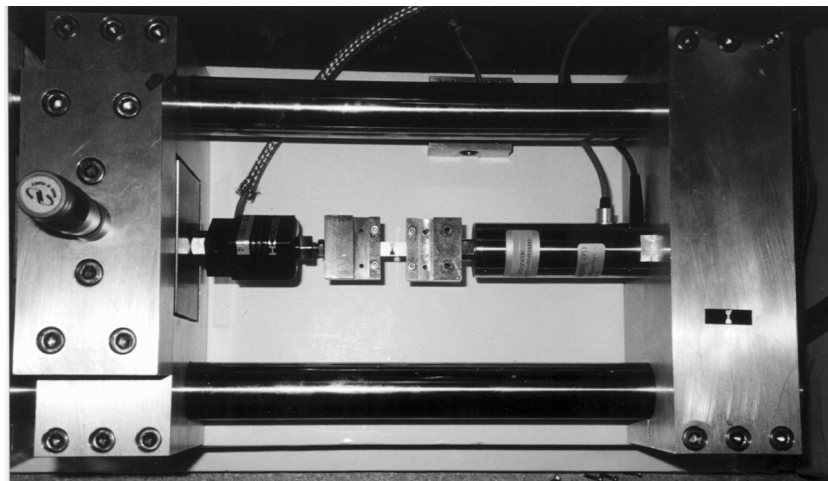


Figure 4-3: Top view of the main components of the custom-designed micromechanical testing system.

closed-loop piezo controller, a signal conditioner and an A/D board located in a control PC. Data acquisition is achieved by LabVIEW software. An optical microscope is mounted directly

overlooking the top of the sample for the purpose of height alignment as well as test monitoring. During testing, the system is kept in a thermally insulating box to eliminate possible effects that could be caused by temperature fluctuations, such as load cell drift or change in thermal expansion coefficients of the components of the system, which could lead to inaccurate measurement of stress or strain.

The load cell has a maximum measurement range of 44.5N and a load resolution of  $\pm 0.2\text{mN}$ . The piezo-actuator has a maximum measurement range of  $60\mu\text{m}$  and a displacement resolution of  $\pm 10\text{nm}$ . The load to stress conversion is given by

$$\text{Stress} = \frac{\text{Load}}{\text{Area}} \quad (1)$$

where  $\text{Area} = 50\mu\text{m} \times \text{thickness}$  is the cross-sectional area of the beam. The displacement to strain conversion is given by

$$\text{Strain} = \frac{\text{GaugeDisplacement}}{\text{GaugeLength}} \quad (2)$$

While we are only interested in the displacement of the gauge section of the specimen, other parts of the system along the stress direction also contribute to the total measured displacement. Strain calibration is done by taking into account the stiffness of the load cell, root section of the specimen, and other compliant parts of the system, in addition to the stiffness of the gauge section of the specimen.

#### 4.1.2.2 Experimental Procedures

Prior to testing, the electronics are energized and left to thermally equilibrate. The load cell is pre-calibrated. The sample stage is adjusted under the optical microscope to eliminate the height difference between the two grips.

The test die is removed from the wafer by gently breaking the two silicon support bridges attached to the die corners, and is then placed on the grips with the beam side facing downward. It is then clamped in place by four screws, two on each side, with care taken to ensure even clamping throughout the process (by monitoring the load response on the LabVIEW screen). Upon securing the die onto the grips, the silicon supports on the two long sides of the die are cut with a hand-held rotary diamond saw. The Al micro beam is now free-standing between the two grips, where one end is attached to the load cell and the other to the piezo. Finally, the system is enclosed in the thermally insulating box and allowed to reach thermal equilibrium before actual testing (The temperature is maintained  $\pm 0.5\text{ }^\circ\text{C}$ ).

Tensile tests are performed by allowing the piezo control voltage to increase (i.e. to elongate the beam) monotonically, while the corresponding load (or stress) response of the beam and hence the stress vs. strain relation is recorded by LabVIEW. For a stress relaxation test, the beam is

quickly loaded to a certain strain first and then held at this constant strain while the resulting load (or stress) change is recorded against time elapsed. For cyclic testing, a triangular waveform is set on the piezo controller in order to cycle the piezo position at a constant displacement rate.

### 4.1.3 Results and Discussion

In this section, we will not review previously reported results.

#### 4.1.3.1 Tensile Test of Pure Al and Al-2%Ti Micro Beams (2 $\mu$ m thick)

From the stress vs. strain curves (Fig. 4-4) of the pure Al and Al-2%Ti micro beams, we find Young's modulus to be about 60GPa, close to the value of 62GPa for bulk Al. The yield strength at 0.2% strain for the pure Al micro beams is about 120MPa. The yield strength at 0.2% strain for the Al-2%Ti micro beams is about 210MPa, about 75% higher than that of pure Al.

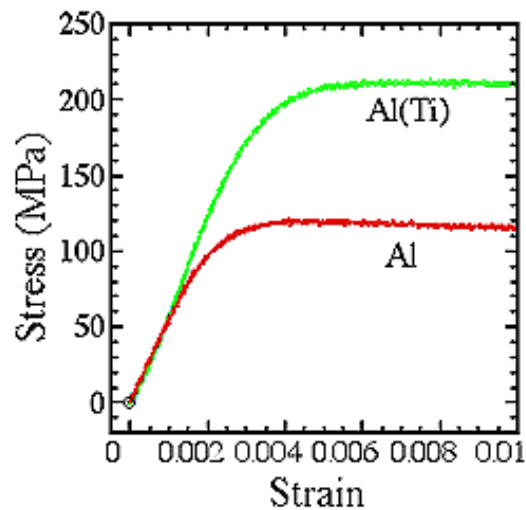


Figure 4-4: Stress vs. Strain curves of pure Al and Al-2%Ti micro beams (2 $\mu$ m thick).

This significant yield strength increase is due to  $Al_3Ti$  precipitates that have formed at grain boundaries. As described earlier in the sample preparation section, the multi-layer was annealed after sputter deposition. TEM studies on the cross-section of the Al/Ti multi-layer (Fig. 4-5) before and after the annealing indicate that Ti had reacted with Al to form  $Al_3Ti$  precipitates along the Al grain boundaries during the heat treatment.  $Al_3Ti$  has a much larger modulus than that of Al. It is known that hard precipitates (in this case,  $Al_3Ti$ ) can block the motion of dislocations in a soft matrix (in this case, Al), and hence increase the amount of stress required to move these dislocations. In effect, this will result in higher yield strength in the Al-2%Ti micro beams than of those made from pure Al.

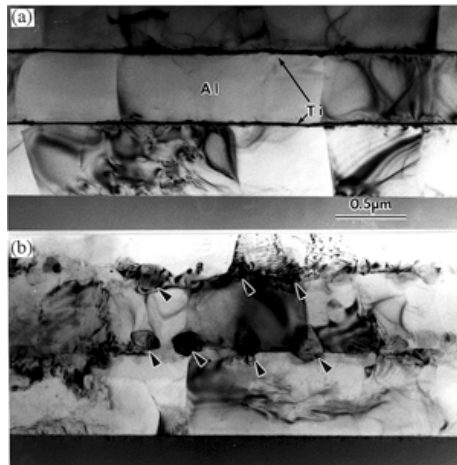


Figure 4-5: TEM cross-sectional view of (a) alternate layers of Ti and Al in the as-deposited Al/Ti multi-layer, (b) Al<sub>3</sub>Ti precipitates formed at Al grain boundaries after annealing. (arrows are pointed to the locations of Al<sub>3</sub>Ti precipitates)

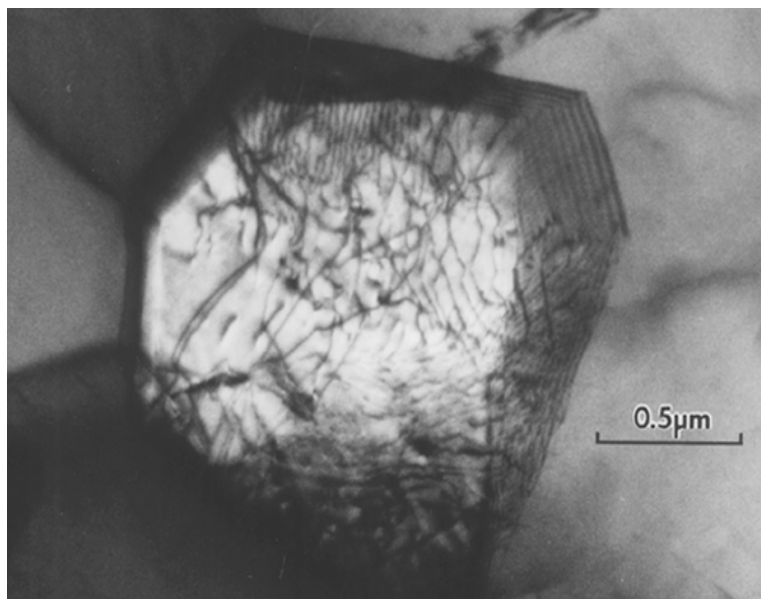


Figure 4-6: TEM bright field image of a grain in a pure Al micro beam, showing dislocations after 0.4% strain.

Our TEM observation on the tested samples also showed a consistent result. The TEM samples were prepared from pure Al and Al-2%Ti beams after 0.4% strain of deformation. The bright field image of the pure Al sample (Fig. 4-6) under a two-beam condition ( $g = 111$ ) reveals many dislocations in the grain that are running rather straight. In the alloyed sample (Fig. 4-7), however, we see a different dislocation pattern, that is, dislocations in the alloyed beams appear

to zigzag or swirl around  $\text{Al}_3\text{Ti}$  precipitates, indicating that their motion was indeed blocked by the presence of the precipitates.

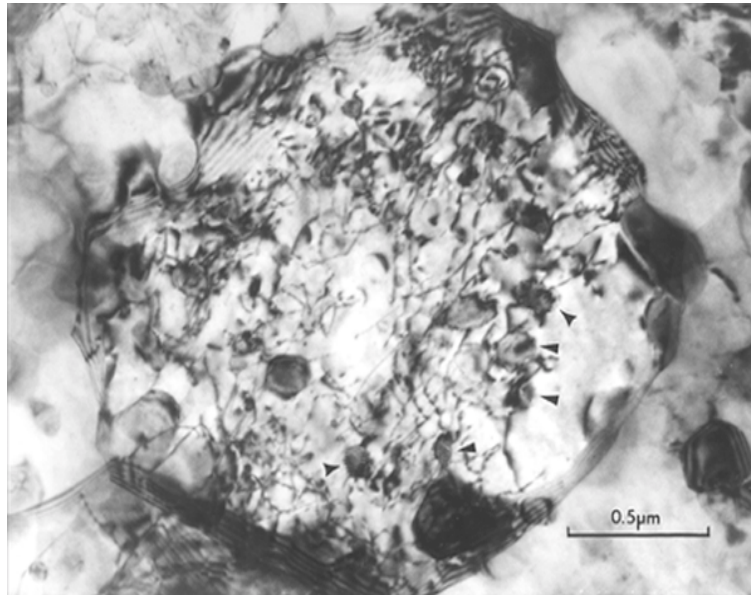


Figure 4-7: TEM bright field image of a grain in an Al-2%Ti micro beam, showing dislocations after 0.4% strain. (arrows are pointed to the locations of  $\text{Al}_3\text{Ti}$  precipitates)

We have therefore demonstrated that we can increase the yield strength of a pure Al free-standing thin film by alloying Al with Ti. In a RF switch application, where both high yield strength and high electrical conductivity are required, choosing Ti as an alloying material for building such MEMS structures offers advantages over pure Al.

#### 4.1.3.2 Stress Relaxation Test of Pure Al and Al-2%Ti Micro Beams (2 $\mu\text{m}$ thick)

In stress relaxation tests, using a strain rate of  $0.25\mu\text{m/s}$ , we first quickly loaded the samples to a strain of  $1.2 \times 10^{-3}$ . Then, holding the strain constant at this value, we recorded the corresponding load change for both the pure Al and the Al-2%Ti micro beams (Fig. 4-8).

For the pure Al micro beams, over a relaxation time of about 9min, the stress dropped from 50MPa to 22MPa, corresponding to a 56% relaxation from the original stress. For the Al-2%Ti micro beams, over the same period of relaxation time, the stress dropped from 50MPa to 44MPa, corresponding to a 16% relaxation.

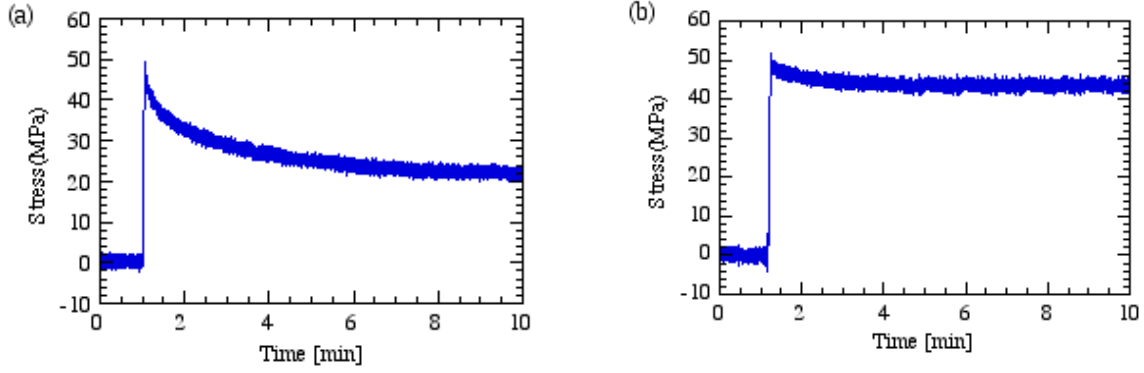


Figure 4-8: Stress relaxation of (a) pure Al, (b) Al-2%Ti micro beams (both 2 $\mu$ m thick).

Stress relaxation has been widely investigated for bulk materials as well as thin films on substrates. Those studies have found that grain boundary sliding is responsible for stress relaxation. However, the amount of stress relaxation from those studies was only a few percent, whereas we found more than 50% for our Al micro beams over the same time period. We have eliminated the possibility of test instrument errors and suggest that grain boundary sliding also accounts for relaxation in free-standing thin films. Qualitatively speaking, we would expect a free-standing thin film to have more grain boundary sliding taking place than a bulk material or a thin film on substrate, again because its top and bottom surfaces are unconstrained. Therefore, the amount of relaxation could be very large compared to bulk, which explains why the pure Al beams exhibit more than 50% of stress relaxation.

In the case of the Al-2%Ti micro beams, we see that the amount of relaxation is significantly less than that of the pure Al. This is probably due to the Al<sub>3</sub>Ti precipitates formed at Al grain boundaries that hinder the grain boundary sliding, thereby decreasing the amount of relaxation compared to the pure Al.

Since our stress relaxation tests were carried out in a stress range below 50MPa, i.e. in the elastic regime, we can attribute the stress relaxation to anelasticity. We can, to first order, model the system as being a spring ( $E_{\infty}$ ) in parallel with a combination of a spring ( $E$ ) and a dashpot ( $\eta$ ) in series. For a constant strain of  $\epsilon_0$ , the relaxed stress is a function of time given by:

$$\sigma(t) = \epsilon_0 \left[ E_{\infty} + E \cdot \exp\left(-\frac{t}{\tau}\right) \right] \quad (3)$$

$$\text{where } \epsilon_0 = \frac{\sigma_{initial}}{E_{\infty} + E} = \frac{\sigma_{final}}{E_{\infty}}, \text{ and } \tau = \frac{\eta}{E}$$

Since the elastic moduli for our pure Al and Al-2%Ti micro beams are nearly the same value, the difference in relaxation time,  $\tau$ , is therefore directly related to  $\eta$ , the damping factor. As we can

imagine, because the  $\text{Al}_3\text{Ti}$  precipitates formed at Al grain boundaries,  $\eta$  is larger in value for the Al-2%Ti micro beams. Consequently, the relaxation time,  $\tau$ , is longer for the Al-2%Ti micro beams, which again explains why the amount of relaxation in the same time period for the pure Al case is larger than for the Al-2%Ti case.

Unfortunately, this simple model could not fit our experimental data very well, and we have therefore proposed a two-Maxwell-element anelastic model, which describes the system as:

$$\sigma(t - t_0) = \varepsilon_0 \left[ E_\infty + E_1 \exp\left(-\frac{t - t_0}{\tau_1}\right) + E_2 \exp\left(-\frac{t - t_0}{\tau_2}\right) \right] \quad (4)$$

$$\text{where } \tau_i = \frac{\eta_i}{E_i}.$$

With this analytical formula, we get a better fit to our experimental data. Our on going study is to investigate different data sets and propose a second mechanism in addition to the grain boundary sliding mechanism.

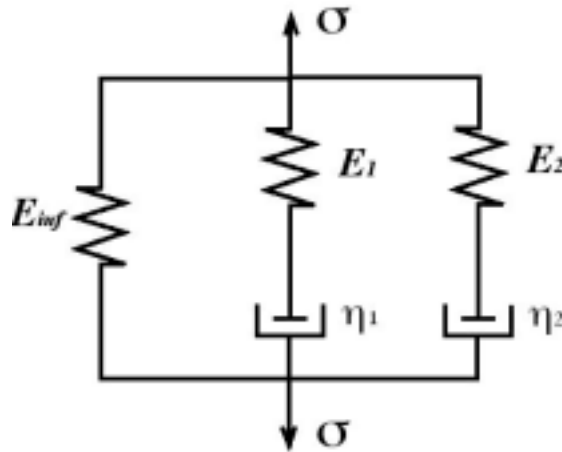


Figure 4-9: Two-Maxwell-element anelastic model.

#### 4.1.3.3 Grain Size Study on Pure Al (2 $\mu\text{m}$ thick)

Stress vs. strain curves of pure Al micro beams annealed at different temperatures (Fig. 4-10) show that as annealing temperature increases, yield strength decreases while ductility increases. The heat-treated samples were each annealed for 1hr in a nitrogen ambient. Corresponding TEM micrographs (Fig. 4-11) revealed that grain sizes increase with annealing temperature. Hence, the result agrees with the Hall-Petch theory on conventional, bulk materials.

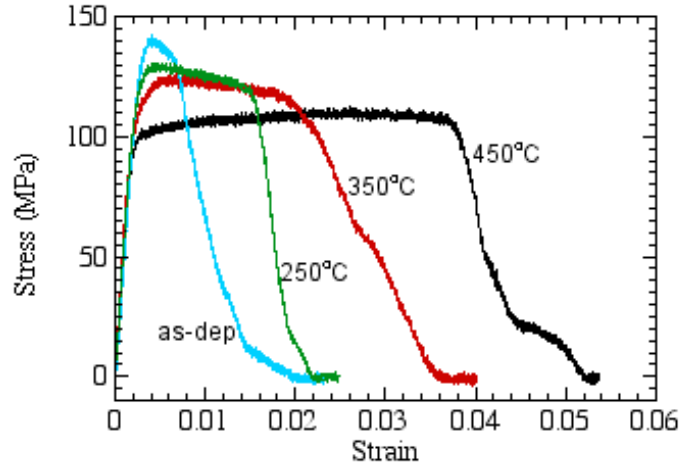


Figure 4-10: Stress vs. strain curves of pure Al micro beams at different annealing temperatures.

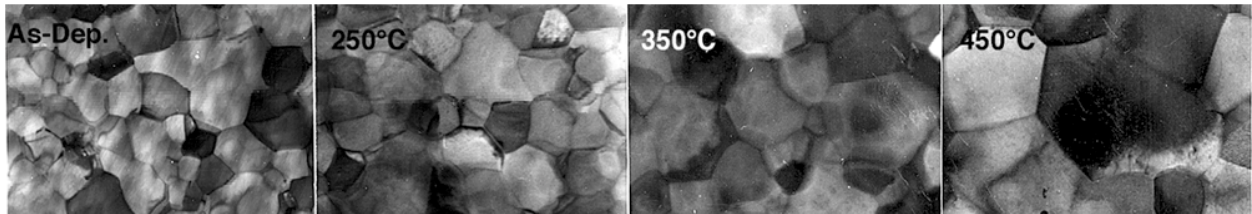


Figure 4-11: TEM micrographs showing grain size increase as increasing annealing temperature.

#### 4.1.3.4 Inhomogeneous Deformation in Pure Al (2 $\mu\text{m}$ thick)

TEM studies revealed inhomogeneous deformation (Fig. 4-12) occurring for the as-deposited, 250 °C and 350 °C annealed samples, but not for the 450 °C fully annealed samples. Inhomogeneous deformation occurs in grains larger in sizes from their neighboring grains. Local thinning (i.e. necking) was observed, corresponding to high contrast in TEM images. Dislocation pileup at grain boundaries of the grains that have undergone inhomogeneous deformation was also observed. To circumvent inhomogeneous deformation, which may be undesirable in a RF switch application, we propose fully annealing. Although this will result in a slightly lower yield strength, we can compensate the yield strength decrease by alloying Al with Ti as described earlier.

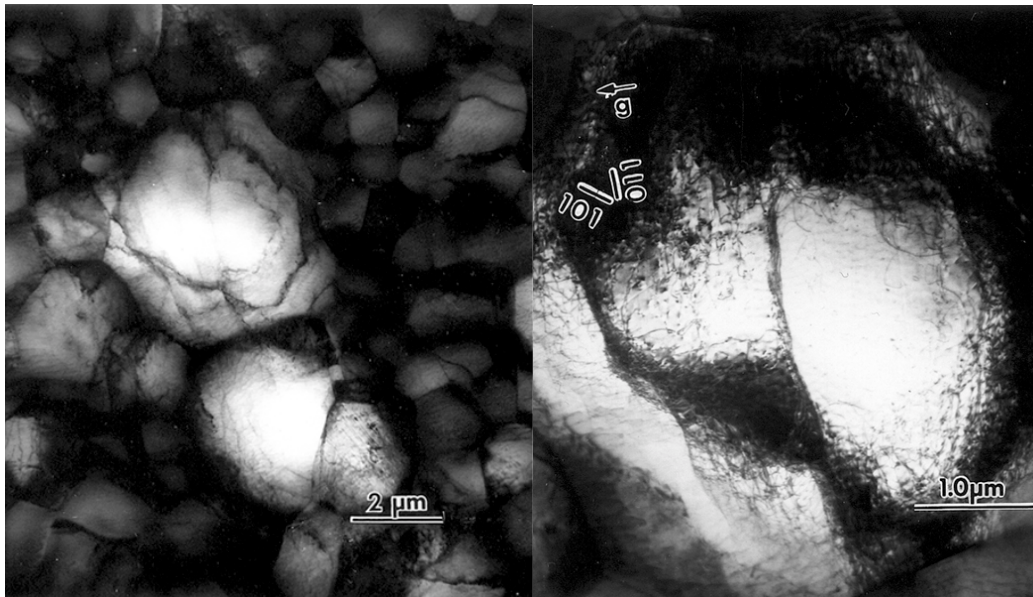


Figure 4-12: TEM bright field images showing inhomogeneous deformation (local thinning) and dislocation pileup at grain boundaries.

#### 4.1.3.5 Preliminary Results on Al/Ti co-Sputtered Films(1μm thick)

On-going work has been directed at studying Al-Ti co-sputtered thin films of different Ti concentrations and different annealing temperature combinations (Fig. 4-13 and 4-14).

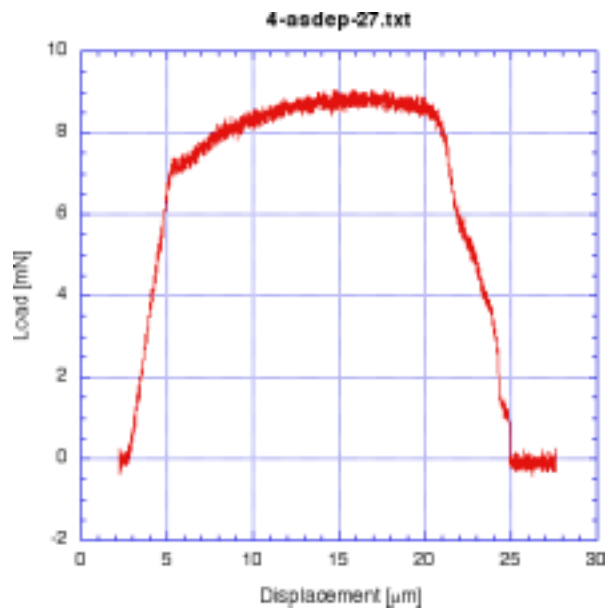


Figure 4-13: Load vs. displacement of Al-1.5%Ti, as-deposited.

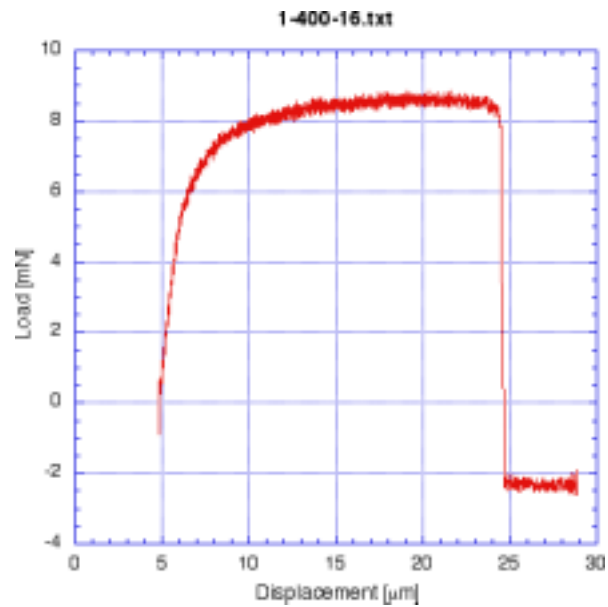


Figure 4-14: Load vs. displacement of Al-1.5%Ti, 400 °C annealed.

## 4.2 In-Situ Stress Monitoring

**Authors: Ping Zhang, Prof. John C. Bravman**

In thin films, especially bi-layer or multi-layer thin films used for MEMS applications, film stress is a key issue to consider. High levels of stress through a film, and stress gradients across a film, may lead to device failure, while stress variations across a wafer may limit the uniformity and/or yield of MEMS devices. While many ex-situ film stress measurement techniques have been developed, in-situ stress monitoring during film deposition remains largely unexplored, especially for films deposited in production-grade equipment. In-situ monitoring will provide valuable information on the evolution and distribution of stress within a film. This should enable deposition conditions to be optimized in order to minimize stress and thus improve device performance.

### 4.2.1 Tunneling Sensor and Initial Modeling

The in-situ stress monitoring device that we have been developing employs a micromachined tunneling sensor with an external feedback control circuitry (Fig. 4-15). The tunneling sensor comprises of two wafer levels. The top Membrane-Wafer level has a micromachined deflection membrane ( $2\text{mm} \times 2\text{mm} \times 0.5\mu\text{m}$ ) made of low stress silicon nitride, gold coated on its backside to form the membrane-electrode; the thin film of interest is deposited on the front side. The bottom Tip-Wafer level has a micromachined tunneling tip set in the center of a shallow square pit, where the tip and its surroundings are coated with gold to form the tip-electrode and the deflection-electrode.

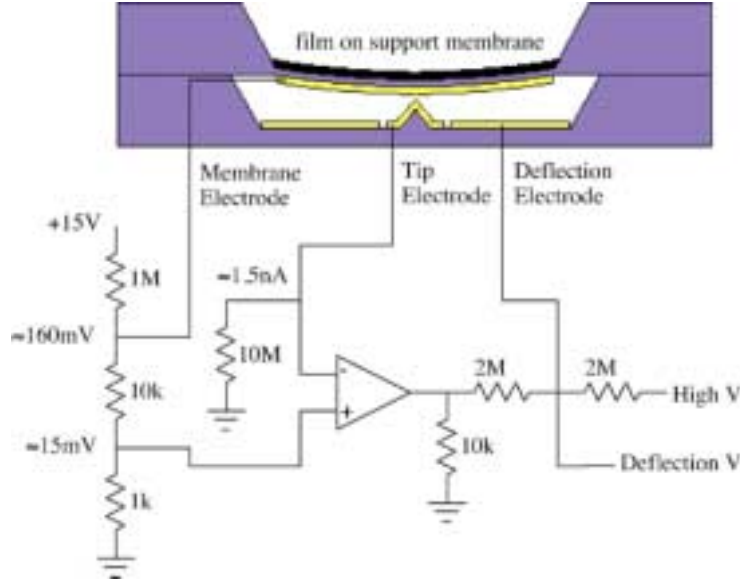


Figure 4-15: Side view schematic of tunneling stress measurement sensor and feedback circuitry.

During stress measurement, the deflection membrane plus thin film of interest is pulled down toward the bottom electrodes by the deflection voltage applied between the membrane-electrode and deflection-electrode. As the tip-to-membrane distance becomes as close as  $10\text{\AA}$ , significant electron tunneling occurs, corresponding to a tunneling current of about  $1.5\text{nA}$ . The feedback control circuit ensures that this current is kept constant, meaning the tip-to-membrane distance is held constant (i.e. a constant center-deflection position). For a change in film stress, the deflection voltage will have to change accordingly in order to maintain this tip-to-membrane position. The deflection voltage change is hence related to the film stress change by the following empirical formula:

$$\left( \frac{\epsilon_0 a^4}{2d^2} \right) V_D^2 = (3.04ta^2h)\sigma + (1.83tEh^3) \quad (5)$$

- where
- $V_D$  = the deflection voltage
  - $\sigma$  = stress
  - $\epsilon_0$  = permittivity of air
  - $d$  = distance between the membrane and deflection electrodes
  - $t$  = total thickness of the deflection membrane and the deposited thin film
  - $h$  = center deflection of the membrane
  - $a$  = half the side length of the square membrane
  - $E$  = average Young's Modulus

#### 4.2.2 Stress Monitoring Device and Ex-Situ Stress Measurement Results

Ex-situ stress measurements were performed on the stress monitoring devices modified from some Infrared Radiation Detectors, which also employ the tunneling sensor part, but with the Absorber-Wafer level removed. To form the stress monitoring device (Fig. 4-16), the tunneling sensor is wire-bonded and packaged and plugged onto a proto board built with feedback circuitry.

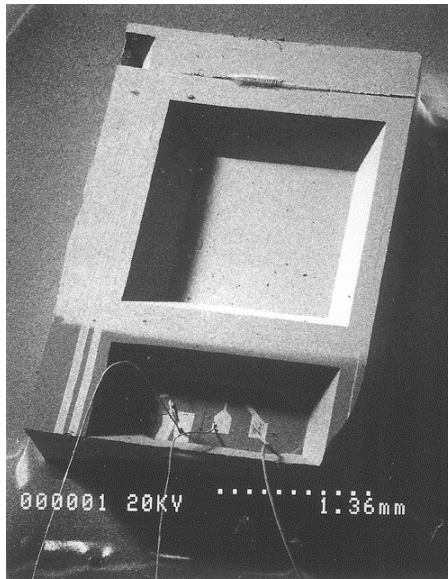


Figure 4-16: Wire-bonded and packaged stress monitoring device.

We sputter deposited Ta onto the deflection membrane and found from tunneling tests that the deflection voltage changed from 48.5V to 59.7V, before and after the Ta deposition. The +11.2V of voltage change corresponds to a stress change of about 0.4GPa, tensile, according to the initial modeling (Fig. 4-17). This stress change agreed with the stress calibrated by Wafer Curvature measurements on blanket Ta films of about 0.5-1GPa.

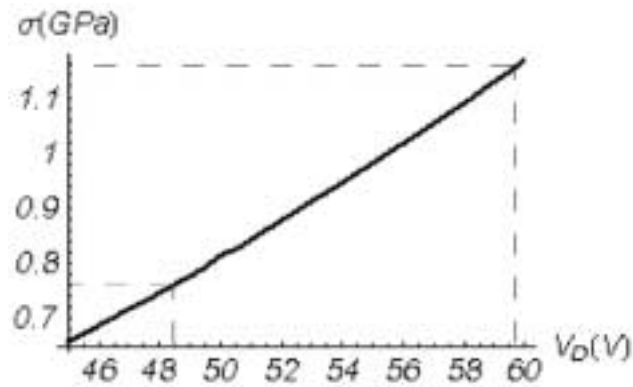


Figure 4-17: Stress vs. deflection voltage curve modeled by equation (5).

### 4.2.3 Fabrication of Dedicated Stress Monitoring Sensor

The fabrication of dedicated stress monitoring sensors uses a set of 7 masks on two wafer levels. There are 302 dies per wafer batch. Details are described in [5]. Unfortunately, processing issues primarily involving the definition of the tips during wet etch and the wafer-scale bonding and dicing at the end of the processing resulted in almost zero yield. Attempts were made to solve the problems.

### 4.2.4 ABAQUS Modeling

Using ABAQUS, we have modeled the deflection membrane/film composite behavior under an applied electrostatic force (Fig. 4-18). Both 3D element (C3D20R) and shell elements (S4R5, S4R8, S4R9) were selected, and results from the two were able to converge. Boundary conditions and initial conditions were also taken into account. Simulation data on center deflection vs. deflection voltage (Fig. 4-19), deflection voltage vs. initial stress (Fig. 4-20), and deflection voltage vs. film thickness (Fig. 4-21) were obtained.

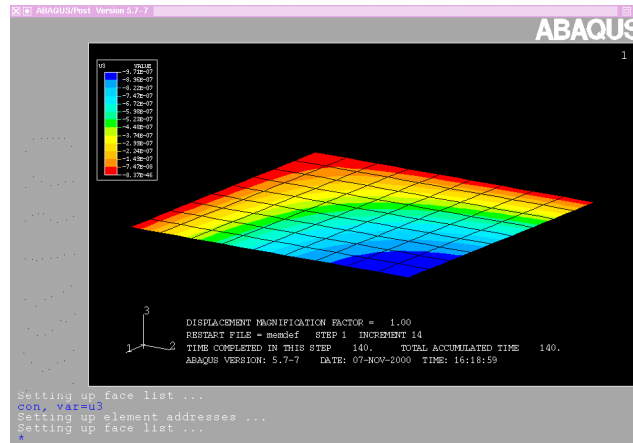


Figure 4-18: ABAQUS modeling of 1/4 membrane, showing center deflection.

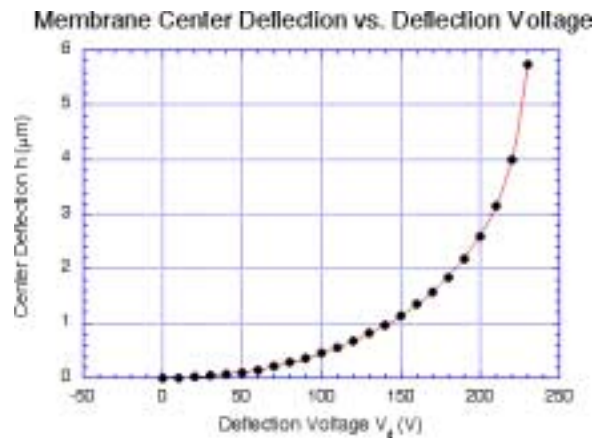


Figure 4-19: ABAQUS modeling result on membrane center deflection vs. deflection voltage (actual sensor).

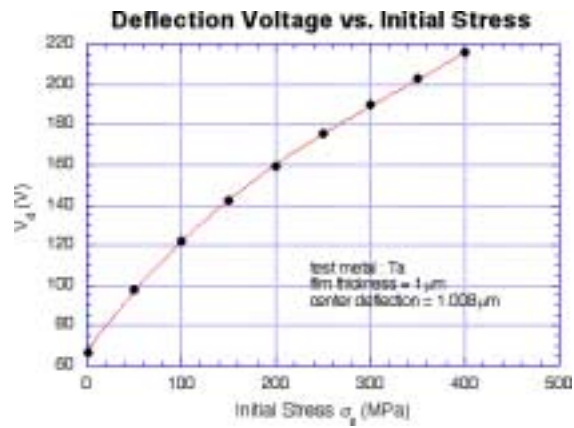


Figure 4-20: ABAQUS modeling result on deflection voltage vs. initial stress (sensor assuming  $1\mu\text{m}$  of center deflection).

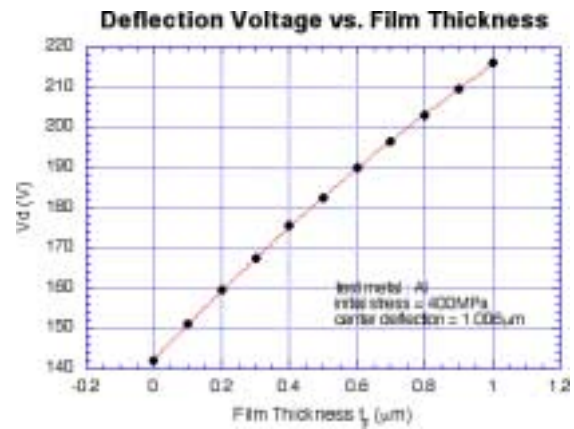


Figure 4-21: ABAQUS modeling result on deflection voltage vs. film thickness (sensor assuming  $1\mu\text{m}$  of center deflection).

### 4.3 References

- [1] Cornella, G., Lee, S., Nix, W. D. and Bravman, J. C. "An Analysis Technique for Extraction of Thin Film Stresses from X-ray Data," *Appl. Phys. Lett.*, vol. 71, #20, 2949-52 (1997).
- [2] Cornella, G., Lee, S., Kraft, O., Nix, W. D. and Bravman, J. C., "Determination of Temperature Dependent Unstressed Lattice Spacings in Crystalline Thin Films on Substrates," *Proceedings of the 1997 MRS Fall Meeting, Boston, MA, USA. Thin-Films - Stresses and Mechanical Properties VII Materials Research Society Symposium Proceedings Vol. 505, 1998, MRS, Warrendale, PA, USA, p. 527-532.*
- [3] Cornella, G., Vinci, R. P., Suryanarayanan Iyer, R., Dauskardt, R. H. and Bravman, J. C., "Observations of Low Cycle Fatigue of Al Thin Films for MEMS Applications," *Proceedings of the 1998 MRS Spring Symposium, San Francisco, CA, USA. Microelectromechanical Structures for Materials Research, Materials Research Society Symposium - Proceedings Vol. 518, 1998, MRS, Warrendale, PA, USA, p. 81-88.*
- [4] Cornella, G., "Monotonic and Cyclic Testing of Thin Film Materials for MEMS Applications," *Ph.D. Dissertation, Stanford University, 1999.*
- [5] Zhang, P., Vinci, R. P., Bravman J. C. and Kenny, T. W., "Thin Film Stress Measurement with a Tunneling Sensor," *Proceedings of the 1998 MRS Fall Meeting - Symposium AA, Materials Science of Microelectromechanical Systems (MEMS), Boston, MA, USA. Materials Research Society Symposium - Proceedings Vol. 546, 1999, p. 45-50.*
- [6] Lee, H.-J., Cornella, G. and Bravman, J. C., "Stress Relaxation of Free-Standing Aluminum Beams for Microelectromechanical Systems Applications," *Applied Physics Letters*, vol. 76, #23, 3415-17 2000.
- [7] Zhang, P., Lee, H.-J. and Bravman, J. C., "Mechanical Tests of Free-Standing Aluminum Micro Beams for MEMS Application," *Mechanical Properties of Structural Films, ASTM STP 1413, American Society for Testing and Materials, West Conshohocken PA, 2001 (submitted).*
- [8] Lee, H.-J., Zhang, P. and Bravman, J. C., "A Study of Plastic Deformation Behavior of Free-standing Aluminum Beams for MEMS Applications," (to be submitted to *Journal of Materials Research*).

## APPENDIX I - LIST OF PUBLICATIONS

### PhD Theses:

Edward Keat Leem Chan, "Characterization and Modeling of Electrostatically Actuated Polysilicon Micromechanical Devices," Stanford University PhD Thesis, November, 1999.

Guido Cornella, "Monotonic and Cyclic Testing of Thin Film Materials for MEMS Applications," Stanford University PhD Thesis, July, 1999.

Kenneth Honer, "Surface Micromachining Techniques for Integrated Microsystems," Stanford University PhD Thesis, January, 2001.

Kenneth Wang, "Level Set Methods for Computational Prototyping with Application to Hemodynamic Modeling," Stanford University PhD Thesis, Expected Date, 2001.

### Journal Publications:

E. K. Chan, K. Garikipati, R. W. Dutton, "Characterization of contact electromechanics through capacitance-voltage measurements and simulations," *Journal of Microelectromechanical Systems*, June 1999; vol. 8, no. 2, pp.208-17.

E. K. Chan, R. W. Dutton, "Comprehensive static characterization of vertical electrostatically actuated polysilicon beams," *IEEE Design and Test of Computers Magazine*, Special Issue on Testing for MEMS, vol 16 no 4, Oct-Dec 1999, pp. 58-65.

E. K. Chan, R. W. Dutton, "Electrostatic micromechanical actuator with extended range of travel," *Journal of Microelectromechanical Systems*, Sept. 2000, vol.9, no.3, pp.321-8.

G. Cornella, S. Lee, W. D. Nix, J. C. Bravman, "An Analysis Technique for Extraction of Thin Film Stresses from X-Ray Data", *Applied Physics Letters*, Nov. 17, 1997, vol.71, no.20, pp. 2949-51.

G. Cornella, J. C. Bravman, and R. P. Vinci, "Monotonic and Cyclic Testing of Thin Film Materials for MEMS Applications", submitted for publication in the *Journal of Micro Electro Mechanical Systems*, July 1999.

Z. K. Hsiau, E. C. Kan, J. P. McVittie, R. W. Dutton, "Robust, Stable, and Accurate Boundary Movement for Physical Etching and Deposition Simulation," *IEEE Trans. Elect. Dev.*, vol. 44, p. 1375, 1997.

H-J. Lee, G. Cornella, J. C. Bravman, "Stress Relaxation of Free-Standing Aluminum Beams for Microelectromechanical Systems Applications," *Applied Physics Letters*, vol. 76, #23, 3415-17 2000.

H-J. Lee, P. Zhang, J. C. Bravman, "A Study of Plastic Deformation Behavior of Free-standing Aluminum Beams for MEMS Applications," (to be submitted to Journal of Materials Research).

Conference Publications:

E. K. Chan, E. C. Kan, R. W. Dutton and P. M. Pinsky, "Nonlinear dynamic modeling of micromachined microwave switches," IEEE Microwave Theory and Techniques Symposium, Denver, June 1997, pp. 1511-14.

E. K. Chan, K. Garikipati, Z. K. Hsiau, R. W. Dutton, "Characterization of electrostatically-actuated beams through capacitance-voltage measurements and simulations", Modeling and Simulation of Microsystems (MSM), Santa Clara, April 1998, pp. 180-5.

E. K. Chan, R. W. Dutton, "Effects of capacitors, resistors and residual charges on the static and dynamic performance of electrostatically-actuated devices," SPIE Symposium on Design, Test and Microfabrication of MEMS/MOEMS, Paris, March 1999.

E. K. Chan, K. Garikipati, R. W. Dutton, "Complete characterization of electrostatically-actuated beams including effects of multiple discontinuities and buckling," Modeling and Simulation of Microsystems (MSM), Puerto Rico, April 1999.

E. K. Chan, R. W. Dutton, "Effect of surface properties on the effective electrical gap of electrostatically actuated micromechanical devices operating in contact," Modeling and Simulation of Microsystems (MSM), San Diego, March 2000.

T. Chen, D.W. Yergeau and R.W. Dutton, "A Common Mesh Implementation for Both Static and Moving Boundary Process Simulations," SISPAD '98, September 2-4, 1998.

G. Cornella, S. Lee, O. Kraft, W. D. Nix, J. C. Bravman, "Determination of Temperature Dependent Unstressed Lattice Spacings in Crystalline Thin Films on Substrates", Materials Research Society Symposia Proceedings, Boston, MA, Dec. 1-5, 1997, Thin-Films-Stresses and Mechanical Properties VII, Symposium (1998), pp. 527-32.

G. Cornella, R. P. Vinci, I. R. Suryanarayanan, R. H. Dauskardt, J. C. Bravman, "Observations of Low Cycle Fatigue of Al Thin Films for MEMS Applications," Proceedings of the 1998 MRS Spring Symposium, San Francisco, CA, USA. Microelectromechanical Structures for Materials Research, Materials Research Society Symposium - Proceedings Vol. 518, 1998, MRS, Warrendale, PA, USA, p. 81-88.

G. Cornella, P. Zhang, R. P. Vinci, R. H. Dauskardt, and J. C. Bravman, "Fatigue Testing of Thin Film Materials for MEMS Applications", Materials Research Society Symposia Proceedings, San Francisco, April 13-17, 1998, Vol. 518, pp. 81.

R. W. Dutton, E. K. Chan, N. M. Wilson, Z. K. Hsiau, S. Shen, "Challenges in process modeling for MEMS", Modeling and Simulation of Microsystems (MSM), Santa Clara, April 1998, pp. 1-4.

K.A. Honer, and G.T.A. Kovacs, "Sputtered Silicon for Surface-Micromachined Structures and Cavities," ASME IMECE '99, Nashville TN, Nov. 14-19, 1999.

K. A. Honer, G. T. A. Kovacs, "Sputtered Silicon for Integrated MEMS Applications," Proceedings of the Solid-State Sensor and Actuator Workshop, Hilton Head, South Carolina, June 4 - 8, 2000, pp. 308 - 311.

X. Qi, S. Shen, Z-K Hsiau, Z. Yu, R.W. Dutton, "Layout-based 3D Solid Modeler of IC Structures and Interconnects including Electrical Parameter Extraction," SISPAD '98, September 2-4, 1998.

K.C. Wang, D. Parker, R.W. Dutton, C.A. Taylor, "Level sets for vascular model construction in computational hemodynamics," ASME Summer Bioengineering Conference, Big Sky, Montana, 1999, pp. 721-722.

K.C. Wang, C.A. Taylor, Z. Hsiau, D. Parker, R.W. Dutton, "Level set methods and MR image segmentation for geometric modeling in computational hemodynamics," Proceedings of the 20th Int'l Conference of the IEEE Engineering in Medicine and Biology Society, Hong Kong, 1998, pp. 3079-3082.

N.M. Wilson, Z.K. Hsiau, R.W. Dutton, and P.M. Pinsky, "A Heterogeneous Environment for Computational Prototyping and Simulation Based Design of MEMS Devices", Proceedings of SISPAD, September 2-4, 1998, pp. 153-156.

N. M. Wilson, R. W. Dutton, and P. M. Pinsky, "Utilizing Existing TCAD Simulation Tools to Create Solid Models for the Simulation Based Design of MEMS Devices", Proceedings of International Mechanical Engineering Conference and Exposition, November 15-20, 1998, pp. 565-570.

N. M. Wilson, S. Liang, P. M. Pinsky, and R. W. Dutton, "A Novel Method to Utilize Existing TCAD Tools to Build Accurate Geometry Required for MEMS simulation", Proceedings of Modeling and Simulation of Microsystems, April 19-21, 1999, pp. 120-123.

N. M. Wilson, P. M. Pinsky, and R. W. Dutton, "Investigation of Tetrahedral Automatic Mesh Generation for Finite Element Simulation of Micro-Electro-Mechanical Switches", Proceedings of Modeling and Simulation of Microsystems, April 19-21, 1999, pp. 305-308.

N. M. Wilson, P. M. Pinsky, and R. W. Dutton, "Integration of TCAD Tools into CAD Tools for MEMS", United States Association of Computational Mechanics Conference, August 4-6, 1999, pp. 230-231.

N. M. Wilson, K. Wang, D. Yergeau, and R. W. Dutton, "GEODESIC: A New and Extensible Geometry Tool and Framework with Application to MEMS", Proceedings of Modeling and Simulation of Microsystems, March 27-29, 2000, pp. 716-719.

N. M. Wilson, D. Yergeau, R. W. Dutton, "Internet Based Modeling of Micro-Electro-Mechanical Systems," International Conference of Computational Engineering & Sciences, August 21-25, 2000, pp. 1330-1334.

P. Zhang, R. P. Vinci, J. C. Bravman, and T. W. Kenny, "Thin Film Stress Measurement with a Tunneling Sensor", Materials Research Society Symposia Proceedings, Boston, Nov. 30 - Dec. 4, 1998, Vol. 546.

P. Zhang, R. P. Vinci, J. C. Bravman, T. W. Kenny, "Thin Film Stress Measurement with a Tunneling Sensor," Proceedings of the 1998 MRS Fall Meeting - Symposium AA, Materials Science of Microelectromechanical Systems (MEMS), Boston, MA, USA. Materials Research Society Symposium - Proceedings Vol. 546, 1999, p. 45-50.

P. Zhang, H-J. Lee, J. C. Bravman, "Mechanical Tests of Free-Standing Aluminum Micro Beams for MEMS Application," Mechanical Properties of Structural Films, ASTM STP 1413, American Society for Testing and Materials, West Conshohocken PA, 2001 (submitted).

## **APPENDIX II – REPRINTS OF SELECTED PAPERS**

E. K. Chan, R. W. Dutton, "Effects of capacitors, resistors and residual charges on the static and dynamic performance of electrostatically-actuated devices," SPIE Symposium on Design, Test and Microfabrication of MEMS/MOEMS, Paris, March 1999.

E. K. Chan, K. Garikipati, R. W. Dutton, "Complete characterization of electrostatically-actuated beams including effects of multiple discontinuities and buckling," Modeling and Simulation of Microsystems (MSM), Puerto Rico, April 1999.

E. K. Chan, K. Garikipati, Z. K. Hsiau, R. W. Dutton, "Characterization of electrostatically-actuated beams through capacitance-voltage measurements and simulations", Modeling and Simulation of Microsystems (MSM), Santa Clara, April 1998, pp. 180-5.

K.A. Honer, and G.T.A. Kovacs, "Sputtered Silicon for Surface-Micromachined Structures and Cavities," ASME IMECE '99, Nashville TN, Nov. 14-19, 1999.

K. A. Honer, G. T. A. Kovacs, "Sputtered Silicon for Integrated MEMS Applications," Proceedings of the Solid-State Sensor and Actuator Workshop, Hilton Head, South Carolina, June 4 - 8, 2000, pp. 308 - 311.

N. M. Wilson, S. Liang, P. M. Pinsky, and R. W. Dutton, "A Novel Method to Utilize Existing TCAD Tools to Build Accurate Geometry Required for MEMS simulation", Proceedings of Modeling and Simulation of Microsystems, April 19-21, 1999, pp. 120-123.

N. M. Wilson, K. Wang, D. Yergeau, and R. W. Dutton, "GEODESIC: A New and Extensible Geometry Tool and Framework with Application to MEMS", Proceedings of Modeling and Simulation of Microsystems, March 27-29, 2000, pp. 716-719.